Distributed normal faulting in the tip zone of the South Alkyonides Fault System, Gulf of Corinth, constrained using ^{36}Cl exposure dating of Late-Quaternary wave-cut platforms.

J. Robertson[a*], G.P. Roberts[a], F. Iezzi[a], M. Meschis[a], D. M. Gheorghiu[b], D. Sahy[c], C. Bristow[d], C. Sgambato[e]

[a]Department of Earth and Planetary Sciences, Birkbeck College, University of London, WC1E 7HX, UK.

[b] Scottish Universities Environmental Research Centre, Scottish Enterprise Technology Park, Rankine Avenue, Glasgow, G75 0QF, UK

[c] British Geological Survey, Keyworth, Nottingham, NG12 5GG, UK

[d]Arcadis Consulting Ltd, London, UK

[e] Institute for Risk and Disaster Reduction, University College London, Gower Street, Kings Cross, London, WC1E 6BS UK

Corresponding author: Jenni Robertson (j.robertson@praxisuk.co.uk)

Abstract

The geometry, rates and kinematics of active faulting in the region close to the tip of a major crustal-scale normal fault in the Gulf of Corinth, Greece, are investigated using detailed fault mapping and new absolute dating. Fault offsets have been dated using a combination of $^{234}U/^{230}Th$ coral dates and *in situ* ^{36}Cl cosmogenic exposure ages for sediments and wave-cut platforms deformed by the faults. Our results show that deformation in the tip zone is distributed across as many as eight faults arranged within ~700 m across strike, each of which deforms deposits and landforms associated with the 125 ka marine terrace of Marine Isotope Stage 5e. Summed throw-rates across strike achieve values as high as 0.3-1.6 mm/yr, values that are comparable to those at the centre of the crustal-scale fault (2-3 mm/yr from Holocene palaeoseismology and 3-4 mm/yr from GPS geodesy). The relatively high deformation rate and distributed deformation in the tip zone are discussed in terms of stress enhancement from rupture of neighbouring crustal-scale faults and in terms of how this should be considered during fault-based seismic hazard assessment.

1. **Introduction**

Understanding the deformation that occurs at the tips of normal faults is important because (a) it contributes to knowledge on fault growth and linkage (e.g. Cowie and Shipton, 1998; Peacock and Sanderson, 1991; McLeod et al., 2000; Peacock, 2002), (b) has the potential to inform fault-based seismic hazard analysis about fault connectivity and maximum rupture extent (Scholz and Gupta, 2000), and (c) influences our understanding of fluid connectivity or otherwise of faulted hydrocarbon reservoirs (Yielding et al., 1996). One of the key observations from studies on tip-zone deformation is that the shape of the displacement gradients differs between isolated and interacting faults as a result of perturbation to the surrounding stress field (Peacock and Sanderson, 1991; Willemse et al., 1996; Cartright and Mansfield, 1998; Cowie and Shipton, 1998; Scholz and Lawler, 2004). In particular, steeper displacement gradients occur close to fault tips where adjacent faults are in close proximity (Gupta and Scholz, 2000). However, it is not known how these steep displacement gradients develop through time, whether displacement is always localised on a single fault or spread across several fault strands, and how tip deformation should be incorporated into studies of seismic hazard. To address these questions, this paper provides measurements of deformation rates across all faults within a tip zone over timescales that allow one to recognise how many individual faults are active simultaneously.

Our interest was raised for this topic because we note that at the tips of some crustal-scale faults, distributed faulting dominates as networks of splay faults that form at acute angles to the main fault (McGrath and Davison, 1995; Perrin et al., 2016) (Figure 1). It is unclear whether these fault patterns and the resultant deformation can be more complex where the tips of two crustal-scale faults overlap along strike and interaction occurs between neighbouring faults (Gupta and Scholz, 2000). Moreover, although typically fault displacement decreases to minimal values toward the tip (Cowie and Roberts, 2001), a shared tip zone can host high displacement gradients relative to the main fault (Peacock and Sanderson, 1991; 1994; Schlische et al., 1996) and it is unclear if this is accommodated by deformation spread across multiple faults or localised on a single fault.

A detailed analysis of the deformation within a fault tip zone has the capacity to contribute to fault-based seismic hazard assessment (e.g. Pace et al., 2016). If tip zones contain relatively-high displacements, distributed across multiple faults, or localised on a single fault, this may influence whether ruptures can cross the tip zone onto other neighbouring faults (e.g. Field et al. 2014), influencing estimates of maximum earthquake magnitude (Wells and Coppersmith, 1994). However, the lack of measured displacement data within tip zones means that historic fault-based seismic hazard approaches typically rely on throw/slip rate data from outside the tip zone and the assumption that displacement gradients decrease toward the tips according to pre-ordained fault shapes (Faure Walker et al., 2018). The above assumptions produce significant uncertainty in Probabilistic Seismic

Hazard Assessment (PSHA) (Pace et al., 2016), and have been shown to result in large differences between calculations of recurrence intervals and ground-shaking exceedance probabilities for different fault geometries (Faure Walker et al., 2018). Constraining the rates of deformation at multiple locations along a fault, including within the tip-zone, is therefore a vital component of reducing the uncertainty in PSHA. Furthermore, this may be particularly important if this analysis is carried out in an area where overlapping tip zones occur; higher displacement gradients, and consequently slip/throw rates, may mean that cumulative slip rates may be relatively high, even when compared to 'on fault' values.

One of the main challenges to gaining insights of how tip-zone deformation accumulates through time, over timescales relevant to earthquake rupture, is to derive knowledge of the timescales over which faulting occurs. Existing approaches use measurements of vertical displacement, coupled with the ages of offset strata/landforms (e.g. Sieh et al. 1989; Armijo et al. 1991; Roberts and Michetti, 2004; Galli et al., 2008; Schlagenhauf et al., 2010, Mozafari et al. 2019; Robertson et al., 2019). In tip zones where distributed faulting dominates and slip-rate along individual faults may be (a) relatively low, and (b) difficult to detect, it may be advantageous to concentrate on techniques that average the slip over relatively long time periods. Investigations using deformed Quaternary marine terraces and their associated wave-cut platforms (e.g. Armijo et al., 1996; Roberts et al., 2009, Roberts et al., 2013; Binnie et al., 2016; Jara-Munoz et al., 2017; Meschis et al., 2018; Robertson et al., 2019) allow deformation rates to be measured over 10^{4-5} years, and therefore displacement associated with the very low slip rates of individual tip-zone faults can be resolved.

The western tip area of the north dipping South Alkyonides Fault System (SAFS) (Morewood and Roberts, 1997), located on the Perachora Peninsula (eastern Gulf of Corinth, Greece) provides an opportunity to study the throw rate, 'off-fault' deformation and possible interaction with neighbouring faults. A set of distributed faults at Cape Heraion, in the far west of the Perachora Peninsula, represents the western tip zone of the SAFS (Morewood and Roberts, 1997) (Figure 2). While this area has been studied before (Morewood and Roberts, 1997), this study lacked the detailed mapping of displacement gradients along individual faults, and the age constraints needed to be able to fully examine the rates and spatial variation of deformation. Morewood and Roberts (1997) identified faulted offsets of what they claim is a single marine terrace. Others have made an alternative interpretation where marine terraces at different elevations are not faulted, but instead date from different sea-level highstands (Leeder et al., 2003; Leeder et al., 2005). This disagreement could not be resolved, because although some age constraints were available from $^{234}U/^{230}Th$ dating of corals (Vita-Finzi et al., 1993, Leeder et al., 2003; Leeder et al., 2005; Roberts et al., 2009; Houghton, 2010), ages were not available for marine terrace deposits at different elevations.

Our breakthrough reported herein, is that our detailed mapping revealed that the coral-bearing strata can be mapped along strike into wave-cut platforms, and wave-cut platforms can be dated using *in situ* ^{36}Cl cosmogenic exposure studies (Robertson et al. 2019). Here we test the hypothesis of Morewood and Roberts (1997) of a single, faulted palaeoshoreline by (i) constraining the ages of marine terrace deposits and landforms at different elevations, (ii) calculating individual and cumulative fault throw values and, (iii) exploring how these vary spatially within the tip zone and how they compare to other normal fault tip zones. The results of these analyses are combined with those from Coulomb stress change modelling to explore the interaction of the tip of the SAFS with neighbouring faults. These findings are then discussed in the context of fault-based probabilistic seismic hazard assessment.

2. **Background**

2.1 *Tectonic setting*

The Perachora Peninsula is located within the eastern Gulf of Corinth (Figure 2), one of the world's fastest extending rift systems, with extension rates between <5 mm/yr and 10-15 mm/yr (Davies et al., 1997; Clarke et al., 1998; Briole et al., 2000). The presence of a complex basin structure (e.g. Moretti et al., 2003; Sachpazi et al., 2003; McNeill et al., 2005; Sakellariou et al., 2007; Bell et al., 2009; Nixon et al., 2016; Gawthorpe et al., 2018) is a consequence of extension accommodated along sets of north and south dipping faults. From the Late Quaternary to the present day, north-dipping faults located along the rift system that borders the south of the gulf are predominately responsible for extension, with other faults less active or ceasing activity (Sakellariou et al., 2007; Bell et al., 2009; Roberts et al., 2009; Nixon et al., 2016; Fernandez-Blanco et al., 2019). The north-dipping faults have been shown to have started to dominate the deformation between 340-175 ka (Roberts et al., 2009; Nixon et al., 2016).

The Perachora Peninsula is located between the Alkyonides Gulf to the north and the Lechaion Gulf to the south (Figure 2a). This area is dominated by two crustal-scale, north-dipping, active fault systems, the East Xylocastro Fault System (EXFS) (so named in this study) and the South Alkyonides Fault System (SAFS) (Figure 2a). The EAFS is formed by the East Xylocastro, North Kiato and Perachora faults, located offshore and arranged en-echelon. The linkage of these three faults is unclear (Bell et al., 2009) with some authors suggesting fault connections at depth (Armijo et al., 2006; Nixon et al., 2016) and others suggesting that they are isolated faults (Stefatos et al., 2002; Moretti et al., 2003; Sakellariou et al., 2007). The presence of a set of coherent terraces in the footwall of the East Xylocastro, North Kiato and

Perachora faults (Armijo et al., 2006) combined with the formation of a single depocentre bounding the north-dipping faults on the south side of the gulf (Nixon et al., 2016) has been cited as evidence to support a through-going fault that is connected at depth.

The predominantly onshore, ~40 km long SAFS is comprised of the Pisia, Skinos, East Alkyonides and Psatha faults (Figure 2, Roberts, 1996a; Morewood and Roberts, 1997; 1999; 2001; 2002; Leeder et al., 2005; Roberts et al., 2009). Analysis of the fault system shows that slip vectors converge toward its centre (Roberts, 1996a; 1996b) where a maximum cumulative throw of 2500 m is recorded (Morewood and Roberts, 2002), which decreases toward both tips (Roberts, 1996a; Morewood and Roberts, 1999; Roberts et al., 2009). In the western section of the SAFS, decreasing offset is reflected in deformed Late Quaternary palaeoshorelines and Holocene notches in the footwall (Cooper et al., 2007; Roberts et al., 2009), where uplift rates decrease from 0.52 mm/yr to 0.25 mm/yr from east to west in the most western 5 km of the fault. Roberts et al. (2009) identified that the SAFS experienced an increase in slip rate since ~175 ka by a factor of ~3, suggested to be linked to the cessation of faulting on neighbouring across-strike faults.

Evidence from recent earthquakes combined with Holocene throw and slip rate data provide insight into the activity of faults within the SAFS over decadal to 10^3 year timescales. Specifically, analysis of post-LGM slip on the Pisia fault revealed maximum slip rates of 2.3 mm/yr during the Holocene (Mechernich et al., 2018). Palaeoseismic trenching along the Skinos fault yielded throw rates of 1.2-2.5 mm/yr over ~1500 years (Collier et al., 1998). Two >Ms 6 earthquakes on the 24th and 25th February 1981 are reported to have partially ruptured faults within the SAFS (Jackson et al., 1982; Roberts, 1996a; Collier et al., 1998). Ruptures in bedrock and alluvium that extend for 15-20 km (Jackson et al., 1982; Bornovas et al., 1984; Roberts, 1996a) were observed following the February 1981 earthquakes, with maximum coseismic throw values of 150 cm and 100 cm identified on the Pisia and Skinos faults respectively (Jackson et al., 1982).

The February 1981 earthquake ruptures were mapped to a throw minima along the south of Lake Vouliagmeni (Figure 2c) (Bornovas, 1984; Roberts, 1996a; Morewood and Roberts, 1999) where the “throw and geomorphic expression across [the SAFS] tend to zero” (Morewood and Roberts, 1999) and were used to conclude that the SAFS does not extend beyond the western end of the lake. Consequently, this location was identified as the western fault tip of the SAFS (Morewood and Roberts, 1999, Figure 4a) (‘A’ on Figure 2c). The area to the west of this location, Cape Heraion, is deformed by numerous normal faults, providing an excellent opportunity to explore deformation close to the tip of a normal fault.

2.2 *Cape Heraion, Perachora Peninsula*

The extreme west of the Perachora Peninsula, Cape Heraion, is located beyond the western tip of the SAFS (as defined by Morewood and Roberts, 1999, Figure 2c). It is bounded to the north by the Perachora fault segment, the most eastern fault within the EXFS, and to the south by the south dipping, active Heraion fault (Taylor et al., 2011; Charalampakis et al., 2014; Nixon et al., 2016) (Figure 2a). The geology of Cape Heraion is comprised of a succession of deposits from the Mesozoic to the Late Quaternary with more recent Late Quaternary-Holocene geomorphic features imprinted such as wave-cut platforms and Holocene sea-level notches.

The stratigraphic succession of the Cape comprises Mesozoic basement limestones unconformably overlain by Plio-Pleistocene marls and sandstones that are, in turn, overlain by algal mound bioherms (also known as cyanobacterial mounds) above which a bioclastic shallow-marine coral-bearing sediment occurs (Bornovas, 1984; see Portman et al., 2005 for descriptions of each lithology). The bioherms are dominated by freshwater branched cyanobacterium *Rivularia haematites*, suggested to have formed when the Gulf of Corinth was a lake (Kershaw and Guo, 2001, 2003, 2006). Domal-topped bioherms in the hangingwall and flat-topped bioherms in the footwall suggest they grew up to water level during faulting with restricted vertical growth in the footwall (Kewshaw and Guo, 2006). Subsequent relative sea-level rise resulted in the presence of a marine bioclastic layer above the bioherms (Portman et al., 2005; Roberts et al., 2009) and caves containing marine biota within the bioherms (Kershaw and Guo, 2006). Taken together, the above evidence is suggestive that faults were active during initial freshwater conditions, that were subsequently changed to marine by a relative sea-level rise. However, these lines of evidence are debated by other authors (Leeder et al., 2005; Portman et al., 2005; Andrews et al., 2007), who favour that the bioherms grew in a marine environment.

The observed geomorphology on Cape Heraion resembles that of a ‘stepped’ profile with horizontal surfaces (terraces) separated by steep slopes. The sub-horizontal surfaces are interpreted as marine terraces because they are associated with coralliferous sediments, marine shoreface deposits with Quaternary marine fossils, and wave-cut platforms that are commonly bored by marine lithophagid borings (Morewood and Roberts, 1997, 1999; Leeder et al., 2003; Leeder et al., 2005; Roberts et al., 2009). Quaternary marine terraces typically form during glacio-eustatic sea-level highstands that occur as a response to glacial melting during interglacial periods. At the up-dip terminations of the marine terraces, it is common to find wave-cut notches and platforms that host features such as lithophagid borings and inter-tidal millholes, indicative of formation at palaeoshorelines (Westaway 1993; Griggs et al., 1994; Miller and Mason, 1994; Roberts et al., 2009; Robertson et al., 2019).

Although the marine terraces and intertidal palaeoshoreline indicators are widely accepted, the explanation for the steep slopes separating marine terraces is debated on Cape Heraion. The slopes are interpreted in two ways by different authors: (1) as palaeo- sea-cliffs, cut by wave-action by three successive Quaternary glacioeustatic sea-level highstands (Leeder et al., 2003; Leeder et al., 2005) (Figure 3a); (2) the locations of faults offsetting a single terrace surface, where the up-dip termination of a terrace surface at a slope is the hangingwall cut-off of the marine terrace along the fault (Figure 3b; Morewood and Roberts, 1997). In this latter interpretation, the age of the marine terrace is suggested to be ~125 ka, associated with MIS 5e (Morewood and Roberts, 1997; Roberts et al., 2009) (Figure 3b), with the presence of complex faulting representing a Segment Boundary Zone between the EXFS and SAFS. Both of these explanations rely on age constraints that link a wave-cut platform at ~29 m to MIS 5e (125 ka highstand) dated using U-series coral ages (Vita-Finzi et al., 1993, Leeder et al., 2003; Leeder et al., 2005; Houghton, 2010) (Locality F, Figure 4a), but no age constraints have been available for higher elevation examples, and this is needed to differentiate between the competing hypotheses.

We undertook detailed mapping and dating in an attempt to resolve the debate of successive palaeoshorelines versus faults. In particular, we tried to identify whether the slopes between terrace locations were continuous along strike, consistent with the suggestion that they represent a succession of palaeoshorelines, or whether the offset of the slopes varied along strike and displayed tip zones and relay ramps, suggestive of faulting. Later we present the results of field mapping and dating that supports the hypothesis of Morewood and Roberts (1997) that the observed variation in terrace elevation is as a result of faulting.

The significance of Holocene wave-cut notches cut into the cliffs along the most western point of Cape Heraion has also been the subject of debate (Pirazzoli et al., 1994; Stiros, 1995; Stiros and Pirazzoli, 1998; Kershaw and Guo, 2001; Cooper et al., 2007; Boulton and Stewart, 2015; Schneiderwind et al.,2017a; Schneiderwind et al.,2017b). It is clear that these notches form as a result of the chemical, biological and physical wave action eroding the cliffs in the intertidal zone along palaeoshorelines (Pirazzoli, 1986). The ages of four notches observed on Cape Heraion were dated to between 190-440 A.D. and 4440-4320 A.D. and used to infer coseismic footwall uplift increments of 0.8 m from earthquakes with recurrence intervals of ~1600 years (Pirazzoli et al., 1994). However, 0.8 m has been suggested to be a relatively high value for coseismic footwall uplift (Cooper et al., 2007; Boulton and Stewart, 2015; Schneiderwind et al.,2017b; Meschis et al., 2019). Whatever their mode of formation, we show below that the notches are deformed by active faulting and use this as part of our explanation of the geological history of Cape Heraion.

2.3 *Using marine terraces and wave-cut platforms to obtain age constraints*

Exploring the deformation of marine terraces and wave-cut platforms relies on obtaining age controls for terraces, accurate geomorphic mapping of terrace features and knowledge of the timing and relative elevations of sea-level highstands (Robertson et al., 2019). Existing coral ages on Cape Heraion at localities C, F and H (Figure 4a) dated using $^{234}U/^{230}Th$ dating reveal ages that agree to coral growth during MIS 5e from platforms at 7 m (Roberts et al., 2009), 29 m (Collier et al., 1992; Vita-Finzi et al., 1993; Leeder et al., 2003; Leeder et al., 2005; Dia et al., 2007; Houghton, 2010) and 15 m (Burnside, 2010). To augment these ages, this study provides new coral ages, and *in situ* ^{36}Cl cosmogenic exposure ages for wave-cut platforms, inspired by the work of Stone et al. (1996), that can be mapped along strike onto coral–bearing marine terrace sediments. The ^{36}Cl cosmogenic exposure ages are cross checked against new and existing coral ages.

Integral to studies of Quaternary marine terraces and palaeoshorelines is knowledge of sea-level elevation changes linked to sea-level highstands, and the time when sea-level reached its maximum elevation (e.g. Waelbroeck et al., 2002; Lambeck et al., 2002; Siddall et al., 2003; Grant et al., 2014; Spratt and Lisiecki, 2016). On Cape Heraion existing coral ages constrain three wave-cut platforms to MIS 5e (125 ka sea-level highstand) (Localities C,F and H, Figure 4a). The timing of MIS 5e occurred between 138-116 ka (Muhs and Szabo, 1994; Stirling et al., 1998; Hearty et al., 2007; O'Leary et al., 2013; Dutton et al., 2015), with the majority (80%) of sea-level rise suggested to have occurred prior to 135 ka (Muchs and Szabo, 1994; Gallup et al., 2002). Understanding the elevations and timings of past sea levels is beneficial because it provides an additional check against the ages obtained from ^{36}Cl exposure dating, which should fall within known highstand time periods.

3. **Methods**

3.1 Field mapping

Detailed field mapping and sampling for $^{234}U/^{230}Th$ and *in situ* ^{36}Cl exposure dating was carried out during field campaigns throughout 2015 and 2017. For the field mapping we concentrated on key criteria that would differentiate between the palaeo-sea-cliff versus fault interpretations for the steep slopes between terrace locations. In particular, if the steep slopes are palaeo- sea-cliffs they ought to be continuous along strike (Figure 3b). In contrast, if the steep slopes are fault scarps, they may display relay-zone geometries where it would be possible to walk continuously on a single surface, along strike, around fault tips, up relay ramps onto the higher parts of the same terrace surface (Figure 3b).

In order to constrain the geometries and continuity of the marine terraces (Figure 3), 58 spot-height elevations were measured throughout the field area using a handheld barometric altimeter (3 m vertical error) that was regularly calibrated at sea level. These measurements were supplemented by 40 additional elevation values obtained from spot heights from a 5 m digital elevation model (DEM) (4 m vertical error) in ArcGIS. The combination of spot heights, outer edges and fault trace maps has allowed us to identify displacement gradients, fault tips to individual faults and relay zones separating individual faults. Rupture traces from recent (possibly 1981) faulting were mapped using a barometric altimeter and measured with rulers to identify the vertical offsets (throw) observed in colluvium and on bedrock fault scarps and the horizontal extension observed from piercing points. This was carried out as per the approach outlined in Iezzi et al. (2018).

3.2 $^{234}U/^{230}Th$ sampling approach and preparation

We focussed our attention on a 0.5-1 m thick coral-bearing, bioclastic layer overlying the bioherms. The bioclastic deposits are comprised of coarse sand and contain corallites of *Cladocora caespitosa*. Whole corallite samples were removed and prepared as per the approach outlined in Roberts et al. (2009). Each corallite sample was split and the septa removed and discarded as septa have been shown to experience greater post-depositional alteration (Roberts et al., 2009; Houghton, 2010). Individual samples were then fragmented and analysed under a binocular microscope for signs of alteration that appear as patches of brown colouration and small crystal growths. The corallites were physically cleaned using a scalpel to remove areas of alteration and any sediment and then placed in 10% hydrochloric acid for 2-3 seconds after which they were immediately rinsed in ultrapure water. This process was repeated until all signs of alteration were removed. Following this process fragments from each corallite were analysed for $^{234}U/^{230}Th$ as per the method detailed in Crémière et al. (2016).

3.3 ^{36}Cl sampling approach and preparation

For ^{36}Cl dating we focussed our attention on wave-cut platforms that could be mapped along and across strike into the coral-bearing, bioclastic layer, suggesting they would be close in age. Obtaining the absolute ages of wave-cut platforms using cosmogenic ^{36}Cl exposure dating relies on (i) sampling from a surface comprised of a calcium-rich lithology that has (ii) experienced minimal erosion and negligible burial, under soil for example, since exposure. This is because the primary production pathway of cosmogenic ^{36}Cl occurs when ^{40}Ca undergoes spallation following the collision of high-energy neutrons at the earth's surface (Dunai, 2010). The spallation reaction is mostly limited to the upper 2 m of rock below exposed surfaces, decreasing exponentially with depth (Licciardi et al., 2008), so high levels of erosion would remove the highest concentrations producing misleadingly-young ages. Other pathways of ^{36}Cl production that must be considered are from low-energy neutrons (Schimmelpfennig et al., 2009) and negative muons, which are the dominant production mechanism for ^{36}Cl at greater depths (Dunai, 2010). We use the approach outlined in Robertson et al. (2019) to identify surfaces that have experienced minimal erosion based on the presence of preserved lithophagid borings and millholes. The depth of lithophagid borings upon formation is between 3-9 cm (Peharda et al., 2015) while millholes, that is, erosional hollows formed by pebble agitation in the intertidal zone, are usually a few centimeters to less than a few decimetres deep. Therefore, the preservation of these features allows us to be confident that we can constrain erosion to less than a few millimetres or centimetres. The low rates of erosion mean that the ^{36}Cl concentration depth profile, determined by the ^{36}Cl production rate depth variation from spallation, will be intact and amenable to age derivation using modelling.

We sampled from wave-cut platforms comprised of differing lithologies at a range of elevations: 62 m, 60 m, 46 m, 42 m and 29 m, including one location where there is an existing age control from $^{234}U/^{230}Th$ coral ages (Locality F, Figure 4a) from sediments formed quasi-contemporaneously with the wave-cut platform (Vita-Finzi et al., 1993; Leeder et al., 2003; Leeder et al., 2005; Houghton, 2010). All samples were removed using a mallet and chisel. Shielding values were noted every 30^{o} of azimuth (as per the method in Dunai, 2010), and used in the age exposure calculations to account for the shielding of cosmogenic rays on the sample site by the surrounding topography (Dunai, 2010). Following removal, samples were analysed in thin section to determine their lithology, washed in distilled water in an ultrasonic bath, then crushed and prepared for ^{36}Cl exposure dating using Accelerator Mass Spectrometry (AMS) as per the method outlined by Schimmelpfennig et al. (2009). The data obtained from AMS was input into CRONUScalc (Marrero et al., 2016), an online calculator that uses measured inputs from data such as ^{36}Cl concentration, elemental composition, elevation, shielding, water content and appropriate uncertainties to calculate the age of the samples with uncertainty values attached.

4. **Results**

This section explores the results of our detailed geological mapping of Cape Heraion and the absolute ages obtained from our ^{36}Cl cosmogenic exposure dating and $^{234}U/^{230}Th$

dating. Alongside existing published ages, these new absolute ages are used to constrain the ages of surfaces at different elevations on Cape Heraion in order to show that faulting is responsible for offsetting a marine terrace linked to the 125 ka highstand within MIS 5e. The results of the dating are used to drive throw rate analyses in order to calculate cumulative throw within the tip zone since 125 ka.

4.1 Field mapping

Detailed field mapping reveals complicated, but linked spatial relationships between lithologies, the stratigraphy and geomorphic features on Cape Heraion (Figures 4, 5, Supplementary data 1, which contains a description of the stratigraphy). Wave-cut platform features have been cut into the stratigraphy (Figure 4a) and are widespread throughout the cape at elevations from 6 m to 99 m (Figures 4, 5 and 6). These horizontal to sub-horizontal surfaces exhibit millholes and lithophagid borings, which are particularly well preserved on the platforms composed of bioclastic packstone (Figures 4a, 6f). Associated with the wave-cut platforms, several localities display coastal notches where the wave-cut platforms impinge on steep outcrops. The notches are marked with lithophagid borings, for example close to location B at ~41 m, with another notch observed at ~92 m (Locality J, Figure 4a).

Our mapping suggests that the lithologic, the stratigraphic and geomorphic features can be interpreted as due to the effect of wave-erosion, at the time of wave-cut platform formation, impinging on palaeo- Cape Heraion, characterised at that time by Quaternary sediments onlapping onto an upstanding inlier of Mesozoic limestone (Figure 5b). The lateral stratigraphic variations were denuded by the wave erosion so that the wave cut-platform formed on different stratigraphic units across the mapped area. The stratigraphy, and the wave-cut platform, have been subsequently offset by faulting that, therefore, post-dates the wave-cut platform, the Cladocora-bearing bioclastic sands and the Rivularia-bioherms (Figure 7).

To gain further insights into the faulting, we have studied the steep slopes that occur along the faults, and in particular the breaks of slope (Figure 4a, c). The map pattern produced by the breaks of slopes reveals patterns that resemble displacement variations along the faults, with slip maximum close to the centres of the map traces, and the positions of relay-ramps at fault tips (Figure 4c). Hence, we interpret these breaks of slope to represent hangingwall and footwall cut offs. Cross-sections across the faults are shown in Figure 8. To cross-check the interpretation of fault segmentation in Figure 4c, we used the elevation data shown in Figure 4b to measure the vertical offsets across the faults, checking that relay-ramps and fault tips identified on Figure 4c are marked by decreased vertical offsets (Figure 9). This cross-check confirms that locations where the hangingwall and footwall cut-offs converge in map view (e.g. the relay-ramps and faults tips in Figure 9b) have low or zero vertical offsets, consistent with our fault segmentation model.

As a final check on the geometries of the faults we have compared their displacement (d) to length (L) ratios to those in a global database (Schlische et al. 1996), because $d = \gamma L$, where γ = 0.01-0.1 with a preferred value of 0.03. We have analysed faults where we have identified both fault tips, and faults where we consider that the centre of the fault has been mapped, assuming that the displacement profiles will be symmetrical. We find values of γ between 0.01-0.1 (Table 1), suggesting that the vertical extents of the steep slopes separating terrace locations are consistent with the interpretation that they are fault scarps. The exception is fault 4, which has a d/L ratio that is comparatively higher (0.27), possibly as a result of being linked at depth with faults 1 and 10 (see the individual fault throw profiles in

Figure 9a for faults 1, 4 and 10). Consequently, the combined *d*/L ratio of these three faults is not representative because the fault continues offshore to the west (Figure 4a, b).

We describe the details of the faulting below. With the exception of three faults that strike approximately N-S not considered in this study, all of the faults strike parallel-sub parallel to the average 260^{o} of the SAFS between 230^{o} and 300^{o} (Figures 2, 4). The faults in the north of the cape are all north dipping and exhibit short fault lengths (100-400 m) and offsets of 2-20 m. South of Fault 11 the presence of a north dipping fault is inferred owing to the 20 m offset of bioherms observed along the scarp of fault 11 (Figure 4a, b). Faults along the south of the cape are longer, and extend outside of the mapping area to the east and offshore to the west (faults 1, 17 and 18) (Figures 4a-c, 7a-c). Along the south of the cape, there are four south-dipping faults (1, 4, 10 and 18) (Figures 4b, 7a-c, e, f). The scarp of fault 18 is not accessible and the offset of this fault is a minimum value as its hangingwall is offshore, however, this fault has been mapped by Morewood and Roberts (1999) farther to the east for ~2 km. South dipping faults 1, 4 and 10 appear to be en echelon to one another and exhibit limestone fault scarps that decrease in offset from west to east.

Strike and dip values, and, where visible, fault striations were measured along the limestone fault scarps of Faults 1, 2, 10 and 17 (Figure 4d). The fault dip for these faults range between 43-66^{o}. In places faults display evidence of activity in a marine setting, faults 1 and 4 display post-slip marine cementation of submarine screes coating the faults (Scott, 1995). Along north dipping faults 2 and 11, offset algal bioherms have horizontal lines of abundant lithophagid borings at 34 m and 41 m respectively, again suggesting slip pre-dates wave-cut platform formation.

In summary, our geomorphological observations and elevation measurements suggest that a pattern of distributed faulting is visible on Cape Heraion. In the context of the north-dipping SAFS and its approximate E-W strike, the faulting on Cape Heraion displays a set of synthetic and antithetic faults that display a 70^{o} variation in strike. While north-dipping faults are more numerous, they appear to have smaller lengths and offsets compared to the four south dipping faults.

4.2 $^{234}U/^{230}Th$ coral dating

The *Cladocora caespitosa* corallites sampled from Cape Heraion (S6U/Th, S7U/Th) (Figure 4) were removed from within a death assemblage on the 44 m wave-cut platform predominantly composed of friable sediments (Figures 6c, 7a). Results of $^{234}U/^{230}Th$ dating on S6U/Th and S7U/Th reveal growth ages of 137 ka and 136 ka respectively (Figure 8a, Table 2). The age presented for S6U/Th is comprised of the average of three analyses from the same corallite, a fourth age was also obtained from this corallite, but we have excluded it as the age of 173.7 ky suggests that it is an outlier and not representative of the age of the corallite (Table 2). The average age of sample S7U/Th is obtained from six analyses from the same corallite (Table 2). The $^{234}U/^{230}Th$ coral ages support growth during MIS 5e and are similar to existing coral growth ages from Cape Heraion (Figure 8a; Vita-Finzi et al., 1993; Leeder et al., 2005; Roberts et al., 2009; Burnside, 2010; Houghton, 2010). Note that all samples have relatively high values of $\delta^{234}U$ of 191-214 (a common way to represent the initial activity ratios of $^{234}U/^{238}U$) compared to modern seawater in the Gulf of Corinth (value of 151; Roberts et al., 2009). It is expected that the samples should have $\delta^{234}U$ values similar to modern sea-water. However, previous studies of coral ages in the Gulf of Corinth, which successfully produced ages of independently-known glacio-eustatic sea-level highstands, have tended to show elevated values (e.g. Collier et al., 1992; Vita-Finzi et al., 1993; McNeill and Collier, 1994; Dia et al., 1997; Leeder et al., 2005; Roberts et al., 2009; Burnside, 2010; Houghton, 2010;

Turner et al., 2010), probably due to the fact that it is a restricted basin with freshwater input. The analyses herein also suggest an age similar to a well-known glacio-eustatic sea-level highstand at ~125 ka. Thus, like previous studies, we use the implied age in our later analysis, despite the relatively high initial activity ratio for our samples.

4.3 ^{36}Cl exposure dating of wave-cut platforms

Cosmogenic ^{36}Cl exposure dating is employed to calculate the time period that sampled surfaces have been subaerially exposed and thus accumulating significantly higher values of ^{36}Cl compared to pre-exposure. Five samples were removed from limestone, bioclastic packstone and algal bioherm wave-cut platforms at different elevations on Cape Heraion (Figures 4a, 6). Our field observations are used to inform the erosion rate used as an input parameter into CRONUScalc, which is used to calculate the exposure age of the samples (see Supplementary data 2 for CRONUScalc input data). The preservation of lithophagid borings and millholes on bioclastic packstone and limestone surfaces (samples 1 and 3) (Figure 6b, f) indicate total erosion values of less than 0.2-0.3 m, whilst samples from the tops of bioherms (samples 2, 4 and 5) are expected to have experienced total erosional values similar with the removed depth of bioclastic packstone/grainstone eroded from the surface of ~0.6 m. These limestone/packstone and bioherm values equate to erosion rates of 0.1 and ~6.0 mm/ky respectively. We note that the 0.1 mm/yr value is the same as that used on limestone wave-cut platforms dated using ^{36}Cl exposure dating in south Crete (Robertson et al., 2019).

Assuming the erosion rates stated above are correct, the ^{36}Cl exposure ages of five samples (Figure 8a, Table 3) are: S1 (limestone, sampled at 60 m) 122 ± 29 ka; S2 (bioherm, sampled at 62m) 108 ± 36 ka; S3 (bioclastic packstone, sampled at 42 m) 109 ± 24 ka; S4 (bioherm, sampled at 46 m) 120 ± 40 ka; S5 (bioherm, sampled at 29 m) 112 ± 35 ka. These results agree with the new and existing U-series ages presented above, suggesting late Quaternary ages close to the age of the 125 ka highstand. The error bars on the ages appear relatively-large, but are comprised of internal (analytical) and external (total) uncertainties that are associated with measured input parameters into CRONUScalc (e.g. H_2O content, elevation, shielding, erosion rates and the production rate; Marrero et al., 2016). Where samples are removed from the same geographical location using the same method, the error values of the input parameters used to calculate the external uncertainty will be very similar (i.e. shielding) or even the same (i.e. production rate, elevation values). Consequently, Marrero et al. (2016) suggests that the external uncertainty value linked to the exposure age may be overestimated when comparing results from the same geographical area, sampled using the same method (see Dunai, 2010). This possible overestimate of uncertainties should be borne in mind when considering the relatively-large error bars associated with the exposure ages, but we have chosen to report the external uncertainties herein.

While the erosion rates used to calculate exposure ages are based upon field observations, we recognise that they form an uncertainty in the ages obtained. Therefore, we examine the sensitivity of the exposure age results to uncertainties in the estimated erosion rates. For samples 1 and 3, we tested erosion rates from 0.1-1 mm/ky and for samples 2, 4 and 5 we tested erosion rates from 5.5-6.5 mm/ky (± 0.5 mm/ky of our estimated erosion rates). The results of these analysis (Supplementary data 3) reveal that the exposure ages may all be allocated to the 125 ka highstand even if our chosen erosion rate is adjusted within the range of ± 0.5 mm/ky. Values for erosion rate larger than this would not be consistent with our field observations of features such as preserved millholes and lithophagid borings. We therefore suggest maximum and minimum values for rates of erosion for samples 1 and 3 of

0.1-1 mm/ky and for samples 2, 4 and 5 of 5.5-6.5 mm/kr. These results support our contention that our erosion rate estimates (samples 1, 3: 0.1 mm/ky and samples 2, 4 and 5: 6 mm/ky) are acceptable.

We suggest that all our exposure ages for the wave-cut platform are associated with MIS 5e, and we discuss this below. Our exposure age results link S1 and S4 and their associated wave-cut platforms to MIS 5e, but the wave-cut platforms that S2, S3 and S5 were removed from, might, at first sight, be linked to either MIS 5c (100 ka highstand) or MIS 5e (125 ka highstand) (Figure 8a). However, using the exposure ages obtained from S1 (60 m) and S4 (46 m), new $^{234}U/^{230}Th$ ages from S6 and S7 (44 m) and existing U-series dating of corals on platforms at 7 m (Roberts et al., 2009), 15 m (Burnside, 2010) and 29 m (Vita-Finzi et al., 1993; Leeder et al., 2003; Leeder et al., 2005; Houghton, 2010) alongside sea-level curve data we suggest that it is more likely that S2 (62 m), S3 (42 m) and S5 (29 m) are associated with MIS 5e (Figure 8c). Our reasoning is that it is difficult to reconcile that platforms at 60 m, 46 m, 44 m, 29 m, 15 m and 7 m were formed by the MIS 5e 125 ka highstand, yet platforms at similar elevations (62 m, 46 m and 29 m) were formed by the MIS 5c 100 ka highstand. This is especially unlikely, given that the maximum sea level during the 100 ka highstand in MIS 5c was -25 m relative to today, and this is 30 m lower than the 5 m relative sea level during the 125 ka highstand of MIS 5e (Siddall et al., 2003) (Figure 8a).

The results of our dating, combined with existing age controls and detailed geological mapping strongly supports that the observed wave-cut platforms on Cape Heraion were all formed during the 125 ka highstand of MIS 5e and have been subsequently faulted since this time (Figure 8c).

4.4 Holocene displacements

Offset Holocene notches and surface faulting that may be associated with the 1981 earthquake suggest occurrence of Holocene faulting on Cape Heraion (Figure 7). An offset notch exists along the base of a cliff at the south west of the cape of as a result of slip on Fault 1 (Figures 4b, 7b). The highest notch is offset by 1.08 m between the footwall and the hangingwall, but it does not appear that a lower notch is also offset (Figure 7b). Our explanation for this is that faulting occurred on Fault 1 following the formation of the upper notch between 4440-4320 B.C. (Pirazzoli et al., 1994) prior to the formation of the lowest notch (at ~1.4 m) between 440-190 A.D.; this may be interpreted as evidence of Holocene faulting on this part of the cape.

Evidence of recent surface faulting may also be present on the north of the cape as a several metre-deep fracture offsetting the bioherms. The fracture (Locality I Figure 4a, and Figure 7d) has a strike of 245^{o}, a horizontal offset of 43 cm, and a direction of opening of 332^{o}, as measured by matching piercing points on both hangingwall and footwall. On Fault 17 between localities J and K (Figure 4a), the occurrence of surface faulting is suggested by a fresh, lichen-free stripe at the base of a carbonate fault plane. These possible surface ruptures, if extrapolated along-strike, cover a distance of ~300 m along the faults. Between localities J and K we observed seven locations that display fresh lichen-free stripes on bedrock fault planes (Figure 7e and f). Bedrock offsets (measured as vertical throw) appear as a light grey stripe at the base of a free face, preserving what appears to be the relative coseismic movement of the colluvium along the fault rupture, ranging from 3-12 cm of throw. In places, the surface rupture has also stepped forward into the hangingwall, located a few centimetres to decimetres away from the carbonate fault plane, to offset the hangingwall colluvial deposits (Figure 7e); vertical offset in the colluvium ranges between 7-28 cm, measured at eight locations between localities J and K (Figure 4a).

As the 1981 earthquakes are the most recent to result in surface ruptures on the Pisia fault (Jackson et al. 1982; Taymaz et al., 1991; Hubert et al., 1996; Roberts, 1996a), and ruptures were reported as close by as along the shore of Lake Vouliagmeni (Bornavas et al. 1984; Figure 2c), we suggest that it is plausible that the ruptures on Cape Heraion, may have also occurred coseismically during the 24th and/or 25th February 1981 earthquakes.

4.6 Throw rates and uplift rates

The absolute ages of wave-cut platforms gained in this paper constrain their formation to the 125 ka highstand within MIS 5e. This means that we can quantify the throw-rate and uplift-rates since 125 ka (Figure 9) to the present day. To constrain the fault geometries, we used elevation data for the footwall and hangingwall cut-offs along the strike of fault traces from the geological and geomorphological map (Figure 4) to construct throw profiles across each fault. Plots of the individual throws for all faults show that faults have maximum offset values of <40 m with two faults exceeding this value (17 and 18) (Figure 9a). When all of the fault throw values and rates are summed across strike they show a pattern of decreasing displacement from east to west (Figure 9c). We emphasise that the data in the grey area on Figure 9c should be interpreted with more caution due to the lack of absolute age control obtained for the wave-cut platform located in the footwall of fault 17 (Figures 4a, 9a), but here we infer that if the notch and small wave-cut platform at ~92-99 m (Locality J, Figure 4a) cut into the footwall of Fault 17 represents the 125 ka palaeoshoreline (Figure 8c, profile 3), we can constrain the throw rate, and we include this in our summed values.

When fault throw and throw rates are plotted separately for the north- and south-dipping faults they mirror the pattern of summed values decreasing from east to west (Figure 9c). It is interesting to note that four south-dipping faults accommodate more throw compared to 14 north-dipping faults with the exception between 1900-1800 m to the west of the ‘on fault’ throw minima (Figure 9c). We postulate that this may be a reflection of the broader faulting pattern within the Gulf of Corinth where the polarity of faulting switched from south-dipping faults to north-dipping faults during the late Quaternary (Roberts et al., 2009; Nixon et al., 2016). Specifically, Roberts et al. (2009) suggested that the north-dipping SAFS experienced an increase in slip at ~175 ka. The short fault lengths and small displacements of the north dipping faults on Cape Heraion may indicate that they may be less mature compared to their south-dipping counterparts. As the summed throw values do not decrease to zero in the mapped area, we suggest that the point of zero vertical offset may lie offshore to the west of Cape Heraion, unless the faulting is actually hard-linked to offshore EXFS.

Another way to consider the results is to explore how throw across active faults has produced spatial variation in uplift relative to present-day sea-level. In other words, the absolute ages of wave-cut platforms, and knowledge of their elevations, allows calculation of spatial variation in uplift rates since 125 ka. Uplift rates since 125 ka from the highest and lowest dated wave-cut platforms are calculated as 0.46 mm/yr (S2, 62 m) and 0.02 mm/yr (Sample P1CWall, 7 m, Roberts et al., 2009) respectively (Figure 4a). If our assertion that the observed notch at 92 m (Locality J, Figure 4a) marks the palaeoshoreline of the 125 ka is correct then a maximum uplift rate of 0.7 mm/yr on Cape Heraion is derived using the 92 m elevation (N.B. these calculations take into account that the sea-level elevation of the MIS 5e highstand was +5 m relative to today’s sea-level). The extreme variability in uplift rate over distances of tens of metres or less precludes simple interpretations of regional tectonic signals in our opinion, as the local uplift is clearly dominated by local faulting (c.f. Leeder et al. 2005).

While the ages obtained in this study and the existing coral U-series link the formation of the wave-cut platforms to the MIS 5e highstand, field observations suggest that some faults were already active prior to MIS 5e. Evidence for this is in the form of (a) marine cementation within submarine screes coating the fault planes on Faults 1 and 4, (b) stratigraphic variations across faults in and below the bioherms, and (c) flat-topped bioherms in the footwall versus domed-topped bioherms in the hangingwall that are suggested to have grown up toward water surface levels during formation (Figure 5) (also observed by Kershaw and Guo, 2006). This evidence suggests that faulting on Cape Heraion was active prior to the beginning of the MIS 5e (~138 ka) and continued throughout the marine stage and beyond. It is possible that along the faults with smaller offsets (such as those in the north) any coseismic offset prior to 125 ka may have either been consequently covered by syn-wave-cut platform sediments or eroded prior to or during the formation of the 125 ka platform; this is particularly plausible given that between the start of MIS 5e at ~138 ka and the highstand at 125 ka any fault offset on the peninsula over this time would have been subject to the erosive forces of rising sea level. Furthermore, coseismic offsets on the faults on the peninsula are expected to be relatively small (a few cm) and therefore easier to erode or obscure with sediment.

5. **Discussion**

Detailed fault mapping and absolute dating on Cape Heraion reveals that the western tip zone of the SAFS accommodates deformation via distributed faulting along synthetic and antithetic faults. Importantly, our findings provide evidence of faulting during the Late Quaternary, specifically over decadal, 10^3 and 10^5 year timescales that is ongoing into the Holocene and perhaps even as recently as 1981. Offset marine terraces and their wave-cut platforms throughout the entire mapped area can be linked to the 125 ka highstand within

MIS 5e. The findings presented in this study, therefore, provide evidence of significant late-Quaternary faulting on Cape Heraion. This outcome is in direct contrast to the findings of Leeder et al. (2003) and Leeder et al. (2005) who refute the notion of displacement of Holocene and late Quaternary shoreline deposits within the study area, and conclude that the Perachora Peninsula is uplifting at a constant, low, uniform rate of 0.2-0.3 mm/yr possibly linked to angle of dip of the subducting African plate beneath the eastern Gulf of Corinth (Leeder et al., 2005) and representing a 'background' uplift rate for the region.

Our fault throw analyses show that summed throw rates in the tip area appear to be relatively high, up to ~1.6 mm/yr (Figure 9), compared to throw and slip rates near the centre of the Pisia and Skinos faults of up to 2.3 mm/yr (Mechernich et al., 2018) and 0.7-2.5 mm/yr (Collier et al., 1998) over the Holocene and 1.2-2.3 mm/yr over the longer term (Collier et al., 1998). From the findings presented here, we conclude that detailed across strike mapping within the tip zone of a fault is imperative in order to constrain accurate rates of long-term faulting that could otherwise be underestimated. We show that the tips of faults should be considered as zones of deformation, rather than localised surface features where a fault stops as they contain multiple active faults.

5.1 *High throw rates on Cape Heraion*

Our findings lead us to question why the throw values obtained in the western tip zone over 125 ka are anomalously high compared to those observed along the localised fault (Figure 10a). Studies of tip displacement gradients commonly suggest high gradients occur where the tips of two faults overlap, as a consequence of the interaction between the stress fields of the faults (e.g. Peacock and Sanderson, 1991; Huggins et al., 1995; Willemse et al., 1996; Cartwright and Mansfield, 1998; Cowie and Shipton, 1998; Gupta and Scholz, 2000;

Ferrill and Morris, 2001; Scholz and Lawler, 2004; Fossen and Rotevatn, 2016). Analysis of an isolated fault tip by Cowie and Shipton (1998) revealed an average tip displacement gradient of 0.018, whereas Cartwright and Mansfield (1998) obtained gradients between 0.0164 to 0.25, in their study of 20 normal faults comprised of a mixture of isolated and interacting faults. In comparison, the tip displacement gradient for the investigated western tip zone of the SAFS is 0.233 (Figure 10b), at the upper range of those observed above.

An explanation of the relatively high summed throw rates on Cape Heraion may be due to fault interaction between the stress fields of the EXFS and the SAFS located along strike to one another and whose eastern and western fault tips overlap (Figure 2a). While this suggestion has been proposed by Morewood and Roberts, (1997), it has not been quantitatively investigated. One way of exploring fault interaction between overlapping faults relies on modelling the calculated Coulomb stress transfer from rupturing a source fault onto a receiver fault. Studies of Coulomb stress transfer (King et al., 1994; Toda et al., 2005) show that following an earthquake, changes in the stress around the slipping patch on the source fault occur that may influence seismicity on neighbouring receiver faults, with positive Coulomb stress transfer bringing a receiver fault closer to failure and negative Coulomb stress transfer resulting in stress shadows. The presence of a stress shadow on the tip zone of a receiver fault may result in deceleration of the propagation of the tip of the receiver fault, which consequently results in displacement accumulating near its interacting tips, causing steeper displacement gradients (Gupta and Scholz, 2000, Figure 14). The deceleration occurs because the fault at the interacting tip must overcome the rupture resistance and stress drop imposed by the adjacent fault (Walsh and Watterson, 1991; Scholz and Lawler, 2004).

We explore whether the location of the eastern EXFS tip zone (Figure 2a) could perturb the stress field of the western tip zone of the SAFS by modelling the Coulomb stress changes following an earthquake on the EXFS (source fault) onto the SAFS (receiver fault) using Coulomb 3.3.01 software. We use the approach and updated code of Mildon et al. (2016) within Coulomb 3.3.01 that allows strike-variable faults to be used, as Coulomb stress transfer is particularly sensitive to changes in the strike of receiver faults (Mildon et al., 2016). An accurate fault trace drawn using Google Earth^{TM} and geometries (dip, strike, rake) of the source (EXFS) and receiver (SAFS) faults (Table 4) were input into the code from Mildon et al. (2016). The source fault was then ruptured to produce a 'standard' earthquake, determined using fault-scaling relationships to calculate the maximum magnitude from the length of the fault rupture (Wells and Coppersmith, 1994). Three source fault rupture scenarios are modelled: (1) the rupture of the SAFS with the exception of the western 2.5 km of the SAFS; (2) the rupture of the entire EXFS; (3) a partial rupture of the EXFS, which involves only the most eastern segment (the Perachora fault) (Figure 2a). Scenario (1) was modelled in order to establish the Coulomb stress transfer imparted from a partial rupture of a fault onto its own tip area (e.g. Roberts 1996). Note that within the Coulomb stress transfer scenarios, the western tip area of the SAFS is defined as the western 2.5 km section of the SAFS, from Point A (Figure 2a) to the west tip of Cape Heraion.

The results of Coulomb stress transfer modelling show stress enhancement on the shallow portions of faults in the region of Cape Heraion, or stress enhancement to greater depths, depending on the exact source to receiver geometry. Rupturing the entire SAFS with the exception of the western 2.5 km section (Scenario 1), results in a significant positive Coulomb stress change of 2 bars onto the entire fault plane of the SAFS western 2.5 km section (Figure 11b). Rupturing the entire EXFS (Scenario (2)) results in the upper and lower 2 km of the SAFS western 2.5 km section experiencing positive stress transfer of 2 bars, while the majority of the western 2.5 km section of the fault plane displays negative stress transfer of up to -2 bars (Figure 11c). Similarly, in scenario (3), rupturing only the Perachora fault segment of the EXFS also results in negative stress transfer of -2 bars over almost all of the western 2.5 km section of the fault with the exception of the upper 1 km, which experiences positive stress transfer values of 1-2 bars (Figure 11d). Overall, the high values of displacement observed on Cape Heraion over 125 ka may be explained by fault interaction between the overlapping tips of the EXFS and the SAFS.

5.2 *Impacts on seismic hazard*

Our findings have implications for fault-based probabilistic seismic hazard assessment (PSHA). We show here that the tip zone of a crustal-scale normal fault can accommodate significant displacement 'off the localised fault', possibly linked to interaction with a neighbouring fault. If these patterns of deformation are assumed to be typical for other normal crustal-scale faults within fault systems that overlap along strike, such as those in the Central and Southern Italian Apennines (Roberts and Michetti, 2004; Papanikolaou et al., 2005; Papanikolaou and Roberts, 2007; Iezzi et al., 2019) and Basin and Range Province, Western USA (e.g. Machette et al., 1991; Anders and Schlische, 1994; Schlische and Anders, 1996, *and references therein*) then our findings may help shed light on how to incorporate slip/throw values into regional datasets, and whether displacements can jump from one major fault to another.

It is known that measurements of slip rate are key inputs into PSHA calculations to gain recurrence intervals and probability of shaking events (e.g. Boncio et al., 2004; Pace et al., 2010; 2016; Valentini et al., 2017). However, due to a sparsity of data, it is common to extrapolate slip rate data from measurements collected on a single location along a fault. This is predominantly done by assuming that displacement decreases towards fault tips (Faure walker et al., 2018). The present study shows that this approach can be problematic, because the interaction between overlapping and interacting fault tips of neighbouring faults might result in anomalously-high displacement in the tip zone, so that throw and slip rates do not simply decrease along strike. Thus, calculation of recurrence rates and the probabilities of given shaking intensities may be in error in such situations.

If our suggestion that high values of displacement in the overlapping tip zones between the EXFS and the SAFS are as a result of fault interaction is correct, then the possibility that earthquake ruptures may jump between the EXFS and SAFS should also be explored. Fault interaction has the capacity to affect rupture sequences whereby seismic events may 'jump' across interacting faults, causing multi-fault earthquakes (e.g. Gupta and Scholz, 2000; Iezzi et al., 2019). For instance, from analysis of the source parameters of the 1981 earthquake sequence, Abercrombie et al. (1995) suggested that the 1981 earthquake sequence might represent a multi-fault rupture between the SAFS and EXFS (or a segment of the EXFS), during which the rupture might have originated offshore and propagated eastward onshore. However, this analysis was carried out without consideration of the distributed faulting reported herein. It is beyond the scope of this paper to confirm or deny whether the presence of distributed faulting may make jumps between co-located faults more or less likely. However, this topic is important because the recent UCERF 3 model (Field et al., 2017) recognises the potential of ruptures to jump between faults that are co-located along strike separated by small distances (5 km), a value similar to those identified by empirical studies of normal faulting earthquakes between 5-7 km (e.g. DePolo et al., 1991; Wesnousky, 2008). The maximum step between the SAFS and EXFS is ~4 km (Figure 2), within the values reported above. Moreover, the observation that anomalously high displacement has accumulated in the Cape Heraion tip zone may be evidence that earthquake ruptures do cross the tip zones, but their presence is only detected if detailed mapping is conducted, and excellent age constraints are available to gain rates of deformation.

We contrast the wealth of observations we provide in the Cape Heraion tip zone with the more typical situation away from sea-level, where transverse bedrock ridges tend to occupy tip zones, and these ridges are made of uniform pre-rift lithologies. In these locations, sparse Quaternary or Holocene sediments may make it difficult to study and gain evidence for active faulting and rates of deformation (e.g. Roberts and Koukovelas, 1996, elsewhere in central Greece; Roberts and Michetti, 2004, Italian Apennines; Zhang et al., 1991; Crone and Haller, 1991; Wu and Bruhn, 1994 western USA, for examples of such transverse bedrock ridges). It may be that smaller distributed displacements remain undiscovered in tip zones between major active faults, and this warrants more investigation, because their study may be one of the few ways to observe whether ruptures cross tip zones to produce hazardous, multi-fault earthquakes.

6. Conclusions

1. Cape Heraion, in the western tip zone of the South Alkyonides Fault System, deforms via a set of distributed faults that are synthetic and antithetic to the 'main fault' and have been active over decadal, 10^3 yr and 10^5 yr timescales. New age constraints using ^{36}Cl cosmogenic exposure dating and ^{234}U/^{230}Th age dating of corals reinforce that the marine terraces and associated wave-cut platforms on Cape Heraion are linked to the 125 ka highstand within MIS 5e rather than a set of terraces from three successive MIS phases.

2. On Cape Heraion, summed throw values (211 – 35 m), throw rates (1.68 – 0.25 mm/yr) and uplift rates (maximum 0.7 mm/yr) appear to exceed those reported on the main fault. These

deformation rates are reflected in an anomalously high displacement gradient of 0.233. Coulomb stress change modelling suggests that this is a consequence of the fault interaction between the overlapping tips of the EXFS and the SAFS.

3. Our findings have implications for probabilistic seismic hazard calculations as they show that the tip zones of crustal-scale faults may host high deformation rates caused by distributed faulting and as such should be mapped in detail across strike. This is particularly important for fault systems worldwide where crustal-scale faults may over lap and where the slip rates are typically propagated along strike from one or two measurements assuming a fault that linearly decreases to zero at the tips.

Acknowledgements

^{36}Cl exposure dating was carried out by the Cosmogenic Isotope Analysis Facility (SUERC, UK) via CIAF grant 9161-1015. ^{234}U/^{230}Th coral age dating was carried out at the Geochronology and Tracers Facility (BGS, UK) via grant IP-1734-0517. We thank Athanassios Ganas and Hellenic Cadastre SA for DEM data via and sincere thanks to Christina Tsimi (NOA) for customising the 5 m digital elevation models for the research area. We also thank Zoe Mildon for sharing her modified Coulomb code and providing support to us when modelling. This study has benefited from discussions with Rebecca Bell, Imperial College, London and from comments from Steve Binnie.

Abercrombie, R. E., Main, I. G., Douglas, A., & Burton, P. W. (1995). The nucleation and rupture process of the 1981 Gulf of Corinth earthquakes from deconvolved broad-band data. *Geophysical Journal International*, *120*(2), 393-405.

Anders, M. H., & Schlische, R. W. (1994). Overlapping faults, intrabasin highs, and the growth of normal faults. *The Journal of Geology*, *102*(2), 165-179.

Andrews, J. E., Leeder, M. R., Portman, C., Rowe, P. J., Smith, J., Kershaw, S., & Guo, L. (2007). Discussion on Pleistocene calcified cyanobacterial mounds, Perachora peninsula, central Greece: a controversy of growth and historyGeological Society, London, Special Publications, Vol. 255, 2006, 53–69. *Journal of the Geological Society*, *164*(5), 1065-1072.

Armijo, R., Lyon-Caen, H., & Papanastassiou, D. (1991). A possible normal-fault rupture for the 464 BC Sparta earthquake. *Nature*, 351(6322), 137.

Armijo, R., Meyer, B. G. C. P., King, G. C. P., Rigo, A., & Papanastassiou, D. (1996). Quaternary evolution of the Corinth Rift and its implications for the Late Cenozoic evolution of the Aegean. *Geophysical Journal International*, *126*(1), 11-53.

Bell, R. E., McNeill, L. C., Bull, J. M., Henstock, T. J., Collier, R. L., & Leeder, M. R. (2009). Fault architecture, basin structure and evolution of the Gulf of Corinth Rift, central Greece. *Basin Research*, *21*(6), 824-855.

Binnie, A., Dunai, T. J., Binnie, S. A., Victor, P., González, G., & Bolten, A. (2016). Accelerated late quaternary uplift revealed by 10Be exposure dating of marine terraces, Mejillones Peninsula, northern Chile. *Quaternary Geochronology*, *36*, 12-27.

Boncio, P., Lavecchia, G., & Pace, B. (2004). Defining a model of 3D seismogenic sources for Seismic Hazard Assessment applications: the case of central Apennines (Italy). *Journal of Seismology*, *8*(3), 407-425.

Bornovas, J., Gaitanakis, P., & Spiridopoulos, A. (1984). *Geological map of Greece, 1:50,000, Perachora Sheet.* Athens: IGME.

Boulton, S. J., & Stewart, I. S. (2015). Holocene coastal notches in the Mediterranean region: Indicators of palaeoseismic clustering?. *Geomorphology*, *237*, 29-37.

Briole, P., Rigo, A., Lyon-Caen, H., Ruegg, J. C., Papazissi, K., Mitsakaki, C., ... & Deschamps, A. (2000). Active deformation of the Corinth rift, Greece: results from repeated Global Positioning System surveys between 1990 and 1995. *Journal of Geophysical Research: Solid Earth*, *105*(B11), 25605-25625.

Burnside, 2010. Unpublished Thesis. University of Glasgow.

Cartwright, J. A., & Mansfield, C. S. (1998). Lateral displacement variation and lateral tip geometry of normal faults in the Canyonlands National Park, Utah. *Journal of Structural Geology*, *20*(1), 3-19.

Charalampakis, M., Lykousis, V., Sakellariou, D., Papatheodorou, G., & Ferentinos, G. (2014). The tectono-sedimentary evolution of the Lechaion Gulf, the south eastern branch of the Corinth graben, Greece. *Marine Geology*, *351*, 58-75.

Cheng, H., Edwards, R. L., Shen, C. C., Polyak, V. J., Asmerom, Y., Woodhead, J., ... & Wang, X. (2013). Improvements in 230Th dating, 230Th and 234U half-life values, and U–Th isotopic measurements by multi-collector inductively coupled plasma mass spectrometry. *Earth and Planetary Science Letters*, 371, 82-91.

Clarke, P. J., Davies, R. R., England, P. C., Parsons, B., Billiris, H., Paradissis, D., ... & Bingley, R. (1998). Crustal strain in central Greece from repeated GPS measurements in the interval 1989–1997. *Geophysical Journal International*, *135*(1), 195-214.

Collier, R. L., Leeder, M. R., Rowe, P. J., & Atkinson, T. C. (1992). Rates of tectonic uplift in the Corinth and Megara basins, central Greece. *Tectonics*, *11*(6), 1159-1167.

Collier, R. E., Leeder, M. R., Trout, M., Ferentinos, G., Lyberis, E., & Papatheodorou, G. (2000). High sediment yields and cool, wet winters: Test of last glacial paleoclimates in the northern Mediterranean. *Geology*, *28*(11), 999-1002.

Collier, R. E., Pantosti, D., D'addezio, G., De Martini, P. M., Masana, E., & Sakellariou, D. (1998). Paleoseismicity of the 1981 Corinth earthquake fault: Seismic contribution to extensional strain in central Greece and implications for seismic hazard. *Journal of Geophysical Research: Solid Earth*, *103*(B12), 30001-30019.

Cooper, F. J., Roberts, G. P., & Underwood, C. J. (2007). A comparison of 103–105 year uplift rates on the South Alkyonides Fault, central Greece: Holocene climate stability and the formation of coastal notches. *Geophysical Research Letters*, *34*(14).

Cowie, P. A., & Roberts, G. P. (2001). Constraining slip rates and spacings for active normal faults. *Journal of Structural Geology*, *23*(12), 1901-1915.

Cowie, P. A., & Shipton, Z. K. (1998). Fault tip displacement gradients and process zone dimensions. *Journal of Structural Geology*, *20*(8), 983-997.

Crémière, A., Lepland, A., Chand, S., Sahy, D., Condon, D. J., Noble, S. R., ... & Brunstad, H. (2016). Timescales of methane seepage on the Norwegian margin following collapse of the Scandinavian Ice Sheet. *Nature communications*, 7, 11509.

Crone, A. J., & Haller, K. M. (1991). Segmentation and the coseismic behavior of Basin and Range normal faults: examples from east-central Idaho and southwestern Montana, USA. *Journal of Structural Geology*, 13(2), 151-164.

Davies, R., England, P. C., Parsons, B., Billiris, H., Paradissis, D., & Veis, G. (1997). Geodetic strain of Greece in the interval 1892–1992. *Journal of Geophysical Research: Solid Earth*, *102*(B11), 24571-24588.

DePolo, C. M., Clark, D. G., Slemmons, D. B., & Ramelli, A. R. (1991). Historical surface faulting in the Basin and Range province, western North America: implications for fault segmentation. *Journal of structural Geology*, *13*(2), 123-136.

Devescovi, M., & Ivesa, L. (2008). Colonization patterns of the date mussel Lithophaga lithophaga (L., 1758) on limestone breakwater boulders of a marina. *Periodicum biologorum*, *110*(4), 339-345.

Dia, A. N., Cohen, A. S., O'nions, R. K., & Jackson, J. A. (1997). Rates of uplift investigated through 230Th dating in the Gulf of Corinth (Greece). *Chemical Geology*, *138*(3-4), 171-184.

Dunai, T. (2010). *Cosmogenic nuclides, principles, concepts and applications in the Earth surface sciences.* Cambridge: Cambridge University Press

Dutton, A., Carlson, A. E., Long, A., Milne, G. A., Clark, P. U., DeConto, R., ... & Raymo, M. E. (2015). Sea-level rise due to polar ice-sheet mass loss during past warm periods. *science*, *349*(6244), aaa4019.

Dutton, A., & Lambeck, K. (2012). Ice volume and sea level during the last interglacial. *science*, *337*(6091), 216-219.

Faure Walker, J. P., Visini, F., Roberts, G., Galasso, C., McCaffrey, K., & Mildon, Z. (2018). Variable Fault Geometry Suggests Detailed Fault-Slip-Rate Profiles and Geometries Are Needed for Fault-Based Probabilistic Seismic Hazard Assessment (PSHA). *Bulletin of the Seismological Society of America*, *109*(1), 110-123.

Fernández-Blanco, D., de Gelder, G., Lacassin, R., & Armijo, R. (2019). A new crustal fault formed the modern Corinth Rift. *Earth-Science Reviews*, 102919.

Ferrill, D. A., & Morris, A. P. (2001). Displacement gradient and deformation in normal fault systems. *Journal of Structural Geology*, *23*(4), 619-638.

Field, E. H., Arrowsmith, R. J., Biasi, G. P., Bird, P., Dawson, T. E., Felzer, K. R., ... & Michael, A. J. (2014). Uniform California earthquake rupture forecast, version 3 (UCERF3)—The time-independent model. *Bulletin of the Seismological Society of America*, *104*(3), 1122-1180.

Field, E. H., Milner, K. R., Hardebeck, J. L., Page, M. T., van der Elst, N., Jordan, T. H., ... & Werner, M. J. (2017). A spatiotemporal clustering model for the third Uniform California Earthquake Rupture Forecast (UCERF3-ETAS): Toward an operational earthquake forecast. *Bulletin of the Seismological Society of America*, *107*(3), 1049-1081.

Fossen, H., & Rotevatn, A. (2016). Fault linkage and relay structures in extensional settings—A review. *Earth-Science Reviews*, *154*, 14-28.

Gallen, S. F., Wegmann, K. W., Bohnenstiehl, D. R., Pazzaglia, F. J., Brandon, M. T., & Fassoulas, C. (2014). Active simultaneous uplift and margin-normal extension in a forearc high, Crete, Greece. *Earth and Planetary Science Letters*, *398*, 11-24.

Galli, P., Galadini, F., & Pantosti, D. (2008). Twenty years of paleoseismology in Italy. *Earth-Science Reviews*, *88*(1-2), 89-117.

Gallup, C. D., Cheng, H., Taylor, F. W., & Edwards, R. L. (2002). Direct determination of the timing of sea level change during Termination II. *Science*, *295*(5553), 310-313.

Grant, K. M., Rohling, E. J., Ramsey, C. B., Cheng, H., Edwards, R. L., Florindo, F., ... & Williams, F. (2014). Sea-level variability over five glacial cycles. *Nature communications*, 5, 5076.

Griggs, G. B., Trenhaile, A. S., Carter, R. W. G., & Woodroffe, C. D. (1994). *Coastal cliffs and platforms* (pp. 425-450). Cambridge University Press, Cambridge, UK.

Gupta, A., & Scholz, C. H. (2000). A model of normal fault interaction based on observations and theory. *Journal of Structural Geology*, *22*(7), 865-879.

Hearty, P. J., Hollin, J. T., Neumann, A. C., O'Leary, M. J., & McCulloch, M. (2007). Global sea-level fluctuations during the Last Interglaciation (MIS 5e). *Quaternary Science Reviews*, *26*(17-18), 2090-2112.

Houghton, 2010. Unpublished Thesis. Birkbeck College, University of London.

Hubert, A., King, G., Armijo, R., Meyer, B., & Papanastasiou, D. (1996). Fault re-activation, stress interaction and rupture propagation of the 1981 Corinth earthquake sequence. *Earth and Planetary Science Letters*, *142*(3-4), 573-585.

Huggins, P., Watterson, J., Walsh, J. J., & Childs, C. (1995). Relay zone geometry and displacement transfer between normal faults recorded in coal-mine plans. *Journal of Structural Geology*, *17*(12), 1741-1755.

Iezzi, F., Mildon, Z., Walker, J. F., Roberts, G., Goodall, H., Wilkinson, M., & Robertson, J. (2018). Coseismic throw variation across along-strike bends on active normal faults: Implications for displacement versus length scaling of earthquake ruptures. *Journal of Geophysical Research: Solid Earth*, *123*(11), 9817-9841.

Iezzi, F., Roberts, G., Walker, J. F., & Papanikolaou, I. (2019). Occurrence of partial and total coseismic ruptures of segmented normal fault systems: Insights from the Central Apennines, Italy. *Journal of Structural Geology*, *126*, 83-99.

Jackson, J. A., Gagnepain, J., Houseman, G., King, G. C. P., Papadimitriou, P., Soufleris, C., & Virieux, J. (1982). Seismicity, normal faulting, and the geomorphological development of the Gulf of Corinth (Greece): the Corinth earthquakes of February and March 1981. *Earth and Planetary Science Letters*, *57*(2), 377-397.

Jara-Muñoz, J., Melnick, D., Zambrano, P., Rietbrock, A., González, J., Argandoña, B., & Strecker, M. R. (2017). Quantifying offshore fore-arc deformation and splay-fault slip using drowned Pleistocene shorelines, Arauco Bay, Chile. *Journal of Geophysical Research: Solid Earth*, *122*(6), 4529-4558.

Kershaw, S., & Guo, L. (2001). Marine notches in coastal cliffs: indicators of relative sea-level change, Perachora Peninsula, central Greece. *Marine Geology*, *179*(3-4), 213-228.

Kershaw, S., & Guo, L. (2003). Pleistocene cyanobacterial mounds in the Perachora Peninsula, Gulf of Corinth, Greece: structure and applications to interpreting sea-level history and terrace sequences in an unstable tectonic setting. *Palaeogeography, Palaeoclimatology, Palaeoecology*, *193*(3-4), 503-514.

Kershaw, S., & Guo, L. (2006). Pleistocene calcified cyanobacterial mounds, Perachora Peninsula, central Greece: a controversy of growth and history. *Geological Society, London, Special Publications*, *255*(1), 53-69.

King, G. C., Stein, R. S., & Lin, J. (1994). Static stress changes and the triggering of earthquakes. *Bulletin of the Seismological Society of America*, *84*(3), 935-953.

Kopp, R. E., Simons, F. J., Mitrovica, J. X., Maloof, A. C., & Oppenheimer, M. (2009). Probabilistic assessment of sea level during the last interglacial stage. *Nature*, *462*(7275), 863.

Lajoie, K. R. (1986). Coastal tectonics. Active tectonics, 95-124.

Lambeck, K., Esat, T. M., & Potter, E. K. (2002). Links between climate and sea levels for the past three million years. *Nature*, 419(6903), 199.

Leeder, M. R., McNeill, L. C., Ll Collier, R. E., Portman, C., Rowe, P. J., Andrews, J. E., & Gawthorpe, R. L. (2003). Corinth rift margin uplift: New evidence from Late Quaternary marine shorelines. *Geophysical Research Letters*, *30*(12).

Leeder, M. R., Portman, C., Andrews, J. E., Collier, R. L., Finch, E., Gawthorpe, R. L., ... & Rowe, P. (2005). Normal faulting and crustal deformation, Alkyonides Gulf and Perachora peninsula, eastern Gulf of Corinth rift, Greece. *Journal of the Geological Society*, *162*(3), 549-561.

Leeder, M. R., Seger, M. J., & Stark, C. P. (1991). Sedimentation and tectonic geomorphology adjacent to major active and inactive normal faults, southern Greece. *Journal of the Geological Society*, *148*(2), 331-343.

Licciardi, J. M., Denoncourt, C. L., & Finkel, R. C. (2008). Cosmogenic 36Cl production rates from Ca spallation in Iceland. *Earth and Planetary Science Letters*, *267*(1-2), 365-377.

Machette, M. N., Personius, S. F., Nelson, A. R., Schwartz, D. P., & Lund, W. R. (1991). The Wasatch fault zone, Utah—Segmentation and history of Holocene earthquakes. *Journal of Structural Geology*, *13*(2), 137-149.

Marrero, S. M., Phillips, F. M., Caffee, M. W., & Gosse, J. C. (2016). CRONUS-Earth cosmogenic 36Cl calibration. *Quaternary Geochronology*, *31*, 199-219.

McGrath, A. G., & Davison, I. (1995). Damage zone geometry around fault tips. *Journal of Structural Geology*, *17*(7), 1011-1024.

McLeod, A. E., Dawers, N. H., & Underhill, J. R. (2000). The propagation and linkage of normal faults: insights from the Strathspey–Brent–Statfjord fault array, northern North Sea. *Basin Research*, *12*(3-4), 263-284.

McNeill, L. C., & Collier, R. L. (2004). Uplift and slip rates of the eastern Eliki fault segment, Gulf of Corinth, Greece, inferred from Holocene and Pleistocene terraces. *Journal of the Geological Society*, *161*(1), 81-92.

McNeill, L. C., Cotterill, C. J., Henstock, T. J., Bull, J. M., Stefatos, A., Collier, R. L., ... & Hicks, S. E. (2005). Active faulting within the offshore western Gulf of Corinth, Greece: Implications for models of continental rift deformation. *Geology*, *33*(4), 241-244.

Mechernich, S., Schneiderwind, S., Mason, J., Papanikolaou, I. D., Deligiannakis, G., Pallikarakis, A., ... & Reicherter, K. (2018). The seismic history of the Pisia fault (eastern Corinth rift, Greece) from fault plane weathering features and cosmogenic 36Cl dating. *Journal of Geophysical Research: Solid Earth*, *123*(5), 4266-4284.

Meschis, M., Roberts, G. P., Robertson, J., & Briant, R. M. (2018). The Relationships Between Regional Quaternary Uplift, Deformation Across Active Normal Faults, and Historical Seismicity in the Upper Plate of Subduction Zones: The Capo D'Orlando Fault, NE Sicily. *Tectonics*, *37*(5), 1231-1255.

Meschis, M., Roberts, G. P., Mildon, Z. K., Robertson, J., Michetti, A. M., & Walker, J. F. (2019). Slip on a mapped normal fault for the 28 th December 1908 Messina earthquake (Mw 7.1) in Italy. *Scientific reports*, 9(1), 1-8.

Mildon, Z. K., Toda, S., Faure Walker, J. P., & Roberts, G. P. (2016a). Evaluating models of Coulomb stress transfer: Is variable fault geometry important?. *Geophysical Research Letters*, *43*(24).

Miller, W. R., & Mason, T. R. (1994). Erosional features of coastal beachrock and aeolianite outcrops in Natal and Zululand, South Africa. *Journal of Coastal Research*, 374-394.

Moretti, I., Sakellariou, D., Lykousis, V., & Micarelli, L. (2003). The Gulf of Corinth: an active half graben?. *Journal of Geodynamics*, *36*(1-2), 323-340.

Morewood, N. C., & Roberts, G. P. (1997). Geometry, kinematics and rates of deformation in a normal fault segment boundary, central Greece. *Geophysical Research Letters*, *24*(23), 3081-3084.

Morewood, N. C., & Roberts, G. P. (1999). Lateral propagation of the surface trace of the South Alkyonides normal fault segment, central Greece: its impact on models of fault growth and displacement–length relationships. *Journal of Structural Geology*, *21*(6), 635-652.

Morewood, N. C., & Roberts, G. P. (2001). Comparison of surface slip and focal mechanism slip data along normal faults: an example from the eastern Gulf of Corinth, Greece. *Journal of Structural Geology*, *23*(2-3), 473-487.

Morewood, N. C., & Roberts, G. P. (2002). Surface observations of active normal fault propagation: implications for growth. *Journal of the Geological Society*, *159*(3), 263-272.

Mozafari, N., SÜMER, Ö., Tikhomirov, D., Ivy-Ochs, S., Alfimov, V., Vockenhuber, C., ... & Akcar, N. (2019). Holocene seismic activity of the Priene-Sazlı Fault revealed by cosmogenic 36 Cl, Western Anatolia, Turkey 2. *Turkish Journal of Earth Sciences*, 28(3).

Muhs, D. R., & Szabo, B. J. (1994). New uranium-series ages of the Waimanalo Limestone, Oahu, Hawaii: implications for sea level during the last interglacial period. *Marine Geology*, *118*(3-4), 315-326.

Nixon, C. W., McNeill, L. C., Bull, J. M., Bell, R. E., Gawthorpe, R. L., Henstock, T. J., ... & Ferentinos, G. (2016). Rapid spatiotemporal variations in rift structure during development of the Corinth Rift, central Greece. *Tectonics*, *35*(5), 1225-1248.

O'Leary, M. J., Hearty, P. J., Thompson, W. G., Raymo, M. E., Mitrovica, J. X., & Webster, J. M. (2013). Ice sheet collapse following a prolonged period of stable sea level during the last interglacial. *Nature Geoscience*, *6*(9), 796.

Pace, B., Peruzza, L., Lavecchia, G., & Boncio, P. (2006). Layered seismogenic source model and probabilistic seismic-hazard analyses in central Italy. *Bulletin of the Seismological Society of America*, *96*(1), 107-132.

Pace, B., Peruzza, L., & Visini, F. (2010). LASSCI2009. 2: layered earthquake rupture forecast model for central Italy, submitted to the CSEP project. *Annals of Geophysics*.

Pace, B., Visini, F., & Peruzza, L. (2016). FiSH: MATLAB tools to turn fault data into seismic-hazard models. *Seismological Research Letters*, 87(2A), 374-386.

Papanikolaou, I. D., & Roberts, G. P. (2007). Geometry, kinematics and deformation rates along the active normal fault system in the southern Apennines: Implications for fault growth. *Journal of Structural Geology*, *29*(1), 166-188.

Papanikolaou, I. D., Roberts, G. P., & Michetti, A. M. (2005). Fault scarps and deformation rates in Lazio–Abruzzo, Central Italy: Comparison between geological fault slip-rate and GPS data. *Tectonophysics*, *408*(1-4), 147-176.

Peacock, D. C. P. (2002). Propagation, interaction and linkage in normal fault systems. *Earth-Science Reviews*, *58*(1-2), 121-142.

Peacock, D. C. P., & Sanderson, D. J. (1991). Displacements, segment linkage and relay ramps in normal fault zones. *Journal of Structural Geology*, *13*(6), 721-733.

Peacock, D. C. P., & Sanderson, D. J. (1994). Geometry and development of relay ramps in normal fault systems. *AAPG bulletin*, *78*(2), 147-165.

Peharda, M., Puljas, S., Chauvaud, L., Schöne, B. R., Ezgeta-Balić, D., & Thébault, J. (2015). Growth and longevity of Lithophaga lithophaga: what can we learn from shell structure and stable isotope composition?. *Marine biology*, 162(8), 1531-1540.

Perrin, C., Manighetti, I., & Gaudemer, Y. (2016). Off-fault tip splay networks: A genetic and generic property of faults indicative of their long-term propagation. *Comptes Rendus Geoscience*, *348*(1), 52-60.

Pirazzoli, P. A. (1986). Marine notches. In *Sea-Level Research* (pp. 361-400). Springer, Dordrecht.

Pirazzoli, P. A., Stiros, S. C., Arnold, M., Laborel, J., Laborel-Deguen, F., & Papageorgiou, S. (1994). Episodic uplift deduced from Holocene shorelines in the Perachora Peninsula, Corinth area, Greece. *Tectonophysics*, *229*(3-4), 201-209.

Portman, C., Andrews, J. E., Rowe, P. J., Leeder, M. R., & Hoogewerff, J. (2005). Submarine-spring controlled calcification and growth of large Rivularia bioherms, Late Pleistocene (MIS 5e), Gulf of Corinth, Greece. *Sedimentology*, *52*(3), 441-465.

Richter, D. K., & Sedat, R. (1983). Brackish-water oncoids composed of blue-green and red algae from a Pleistocene terrace near Corinth, Greece. In *Coated grains* (pp. 299-307). Springer, Berlin, Heidelberg.

Roberts, G. P. (1996a). Noncharacteristic normal faulting surface ruptures from the Gulf of Corinth, Greece. *Journal of Geophysical Research: Solid Earth*, *101*(B11), 25255-25267.

Roberts, G. P. (1996b). Variation in fault-slip directions along active and segmented normal fault systems. *Journal of Structural Geology*, 18(6), 835-845.

Roberts, G. P., & Koukouvelas, I. (1996). Structural and seismological segmentation of the Gulf of Corinth fault system: implications for models of fault growth.

Roberts, G. P., Houghton, S. L., Underwood, C., Papanikolaou, I., Cowie, P. A., van Calsteren, P., ... & McArthur, J. M. (2009). Localization of Quaternary slip rates in an active rift in 105 years: An example from central Greece constrained by 234U-230Th coral dates from uplifted paleoshorelines. *Journal of Geophysical Research: Solid Earth*, *114*(B10).

Roberts, G. P., Meschis, M., Houghton, S., Underwood, C., & Briant, R. M. (2013). The implications of revised Quaternary palaeoshoreline chronologies for the rates of active extension and uplift in the upper plate of subduction zones. *Quaternary Science Reviews*, *78*, 169-187.

Roberts, G. P., & Michetti, A. M. (2004). Spatial and temporal variations in growth rates along active normal fault systems: an example from The Lazio–Abruzzo Apennines, central Italy. *Journal of Structural Geology*, *26*(2), 339-376.

Roberts, S., & Jackson, J. (1991). Active normal faulting in central Greece: an overview. *Geological Society, London, Special Publications*, *56*(1), 125-142.

Robertson, J., Meschis, M., Roberts, G. P., Ganas, A., & Gheorghiu, D. (2019). Temporally constant Quaternary uplift rates and their relationship with extensional upper-plate faults in south Crete (Greece), constrained with 36Cl cosmogenic exposure dating. *Tectonics*.

Sachpazi, M., Clément, C., Laigle, M., Hirn, A., & Roussos, N. (2003). Rift structure, evolution, and earthquakes in the Gulf of Corinth, from reflection seismic images. *Earth and Planetary Science Letters*, *216*(3), 243-257.

Sakellariou, D., Lykousis, V., Alexandri, S., Kaberi, H., Rousakis, G., Nomikou, P., ... & Ballas, D. (2007). Faulting, seismic-stratigraphic architecture and late quaternary evolution of the Gulf of Alkyonides Basin-East Gulf of Corinth, Central Greece. *Basin Research*, *19*(2), 273-295.

Schimmelpfennig, I., Benedetti, L., Finkel, R., Pik, R., Blard, P. H., Bourles, D., ... & Williams, A. (2009). Sources of in-situ 36Cl in basaltic rocks. Implications for calibration of production rates. *Quaternary Geochronology*, *4*(6), 441-461.

Schlagenhauf, A., Gaudemer, Y., Benedetti, L., Manighetti, I., Palumbo, L., Schimmelpfennig, I., ... & Pou, K. (2010). Using in situ Chlorine-36 cosmonuclide to recover past earthquake histories on limestone normal fault scarps: a reappraisal of methodology and interpretations. *Geophysical Journal International*, *182*(1), 36-72.

Schlische, R. W., & Anders, M. H. (1996). Stratigraphic effects and tectonic implications of the growth of normal faults and extensional basins. *Special Papers-Geological Society of America*, 183-203.

Schlische, R. W., Young, S. S., Ackermann, R. V., & Gupta, A. (1996). Geometry and scaling relations of a population of very small rift-related normal faults. *Geology*, *24*(8), 683-686.

Schneiderwind, S., Boulton, S. J., Papanikolaou, I., Kázmér, M., & Reicherter, K. (2017a). Numerical modeling of tidal notch sequences on rocky coasts of the Mediterranean Basin. *Journal of Geophysical Research: Earth Surface*, 122(5), 1154-1181.

Schneiderwind, S., Boulton, S. J., Papanikolaou, I., & Reicherter, K. (2017b). Innovative tidal notch detection using TLS and fuzzy logic: Implications for palaeo-shorelines from compressional (Crete) and extensional (Gulf of Corinth) tectonic settings. *Geomorphology*, *283*, 189-200.

Scholz, C. H., & Gupta, A. (2000). Fault interactions and seismic hazard. *Journal of Geodynamics*, *29*(3-5), 459-467.

Scholz, C. H., & Lawler, T. M. (2004). Slip tapers at the tips of faults and earthquake ruptures. *Geophysical research letters*, *31*(21).

Scott, A (1995). Unpublished Thesis, University of Manchester

Siddall, M., Rohling, E. J., Almogi-Labin, A., Hemleben, C., Meischner, D., Schmelzer, I., & Smeed, D. A. (2003). Sea-level fluctuations during the last glacial cycle. *Nature*, *423*(6942), 853.

Sieh, K., Stuiver, M., & Brillinger, D. (1989). A more precise chronology of earthquakes produced by the San Andreas fault in southern California. *Journal of Geophysical Research: Solid Earth*, 94(B1), 603-623.

Spratt, R. M., & Lisiecki, L. E. (2016). A Late Pleistocene sea level stack. Climate of the Past, 12(4), 1079-1092.

Stefatos, A., Papatheodorou, G., Ferentinos, G., Leeder, M., & Collier, R. (2002). Seismic reflection imaging of active offshore faults in the Gulf of Corinth: their seismotectonic significance. *Basin Research*, *14*(4), 487-502.

Stirling, C. H., & Andersen, M. B. (2009). Uranium-series dating of fossil coral reefs: extending the sea-level record beyond the last glacial cycle. *Earth and Planetary Science Letters*, *284*(3-4), 269-283.

Stirling, C. H., Esat, T. M., Lambeck, K., & McCulloch, M. T. (1998). Timing and duration of the Last Interglacial: evidence for a restricted interval of widespread coral reef growth. *Earth and Planetary Science Letters*, *160*(3-4), 745-762.

Stiros, S. C., & Pirazzoli, P. A. (1995). Palaeoseismic studies in Greece: a review. *Quaternary International*, *25*, 57-63.

Stone, J., Lambeck, K., Fifield, L. K., Evans, J. T., & Cresswell, R. G. (1996). A lateglacial age for the main rock platform, western Scotland. *Geology*, *24*(8), 707-710.

Stuart, F. M., & Dunai, T. J. (2009). Advances in cosmogenic isotope research from CRONUS-EU. *Quaternary Geochronology*, 4(6), 435-436.

Taylor, B., Weiss, J. R., Goodliffe, A. M., Sachpazi, M., Laigle, M., & Hirn, A. (2011). The structures, stratigraphy and evolution of the Gulf of Corinth rift, Greece. *Geophysical Journal International*, *185*(3), 1189-1219.

Taymaz, T., Jackson, J., & McKenzie, D. (1991). Active tectonics of the north and central Aegean Sea. *Geophysical Journal International*, *106*(2), 433-490.

Toda, S., Stein, R. S., Richards-Dinger, K., & Bozkurt, S. B. (2005). Forecasting the evolution of seismicity in southern California: Animations built on earthquake stress transfer. *Journal of Geophysical Research: Solid Earth*, *110*(B5).

Valentini, A., Visini, F., & Pace, B. (2017). Integrating faults and past earthquakes into a probabilistic seismic hazard model for peninsular Italy. *Natural Hazards Earth System Sciences*.

Vita-Finzi, C. (1993). Evaluating late Quaternary uplift in Greece and Cyprus. *Geological Society, London, Special Publications*, *76*(1), 417-424.

Waelbroeck, C., Labeyrie, L., Michel, E., Duplessy, J. C., McManus, J. F., Lambeck, K., ... & Labracherie, M. (2002). Sea-level and deep water temperature changes derived from benthic foraminifera isotopic records. *Quaternary Science Reviews*, 21(1-3), 295-305.

Wells, D. L., & Coppersmith, K. J. (1994). New empirical relationships among magnitude, rupture length, rupture width, rupture area, and surface displacement. *Bulletin of the seismological Society of America*, *84*(4), 974-1002.

Wesnousky, S. G. (2008). Displacement and geometrical characteristics of earthquake surface ruptures: Issues and implications for seismic-hazard analysis and the process of earthquake rupture. *Bulletin of the Seismological Society of America*, *98*(4), 1609-1632.

Wesnousky, S. G., & Biasi, G. P. (2011). The length to which an earthquake will go to rupture. *Bulletin of the Seismological Society of America*, *101*(4), 1948-1950.

Westaway, R. (1993). Quaternary uplift of southern Italy. *Journal of Geophysical Research: Solid Earth*, *98*(B12), 21741-21772.

Wu, D., & Bruhn, R. L. (1994). Geometry and kinematics of active normal faults, South Oquirrh Mountains, Utah: implication for fault growth. Journal of Structural Geology, 16(8), 1061-1075.

Willemse, E. J., Pollard, D. D., & Aydin, A. (1996). Three-dimensional analyses of slip distributions on normal fault arrays with consequences for fault scaling. *Journal of Structural Geology*, *18*(2-3), 295-309.

Yielding, G., Needham, T., & Jones, H. (1996). Sampling of fault populations using sub-surface data: a review. *Journal of Structural Geology*, 18(2-3), 135-146.

Zhang, P., Slemmons, D. B., & Mao, F. (1991). Geometric pattern, rupture termination and fault segmentation of the Dixie Valley—Pleasant Valley active normal fault system, Nevada, USA. *Journal of Structural Geology*, 13(2), 165-176.

Figures

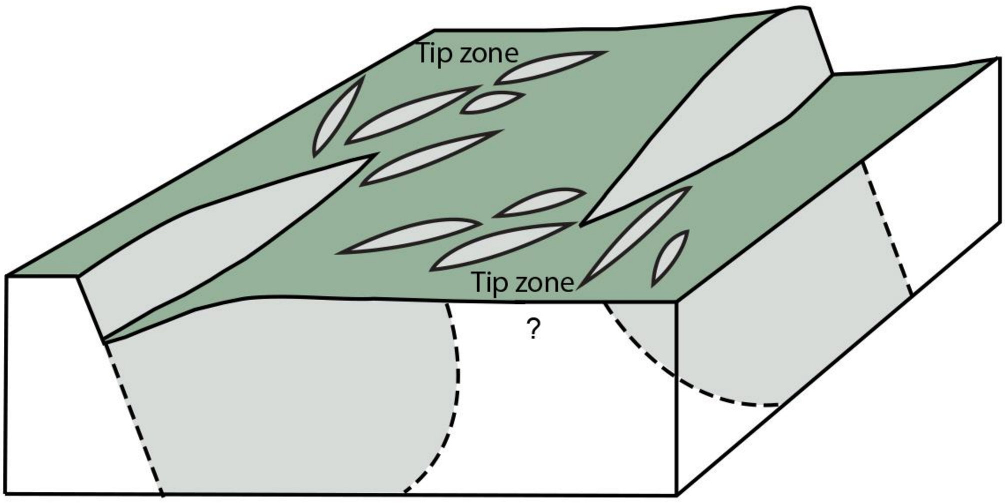

Figure 1: Schematic diagram of a possible tip zone deformation where the tips of two along-strike faults overlap.

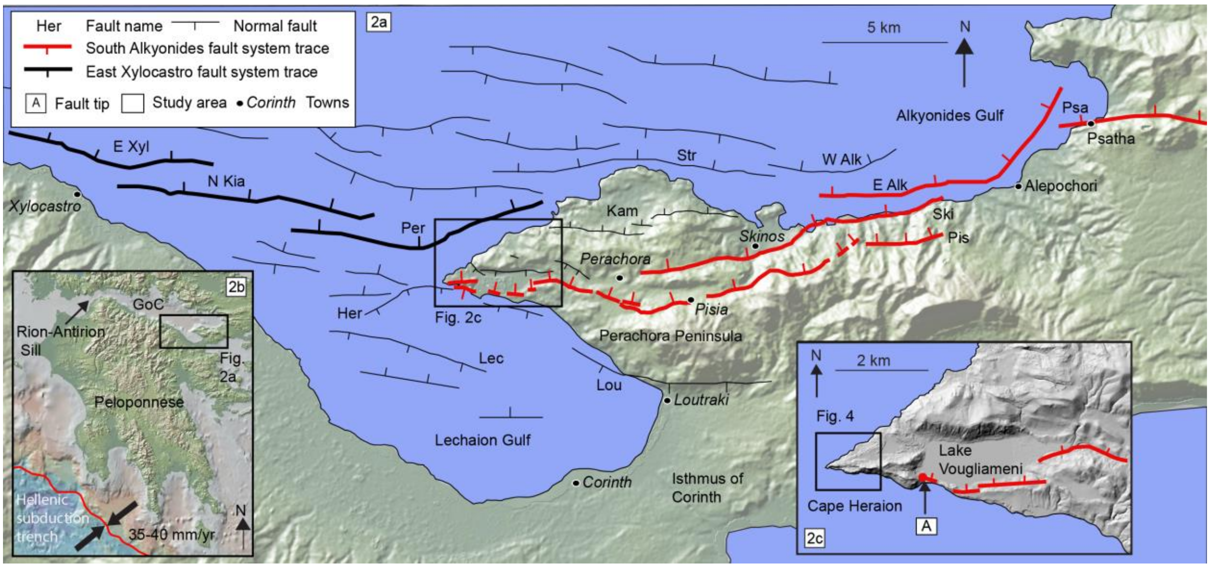

Figure 2: (a) Map of the eastern Gulf of Corinth and the Perachora Peninsula, surface trace of the South Alkyonides Fault system (SAFS) (red) (Morewood and Roberts, 2002), East Xylocastro Fault System (EXFS) trace (Bold) as per Nixon et al., 2016, all other faults as per Nixon et al., 2016. (b) Location of the Gulf of Corinth and Hellenic subduction trench taken from Kreemer and Chamot-Rooke (2004), GPS data from Nocquet (2012). (c) 5 m Digital Elevation Model showing the western surface trace of the SAFS as per Morewood and Roberts (2002) and Cape Heraion. 'A' marks the location of the 'on-fault' tip of the SAFS (Morewood and Roberts, 1999).

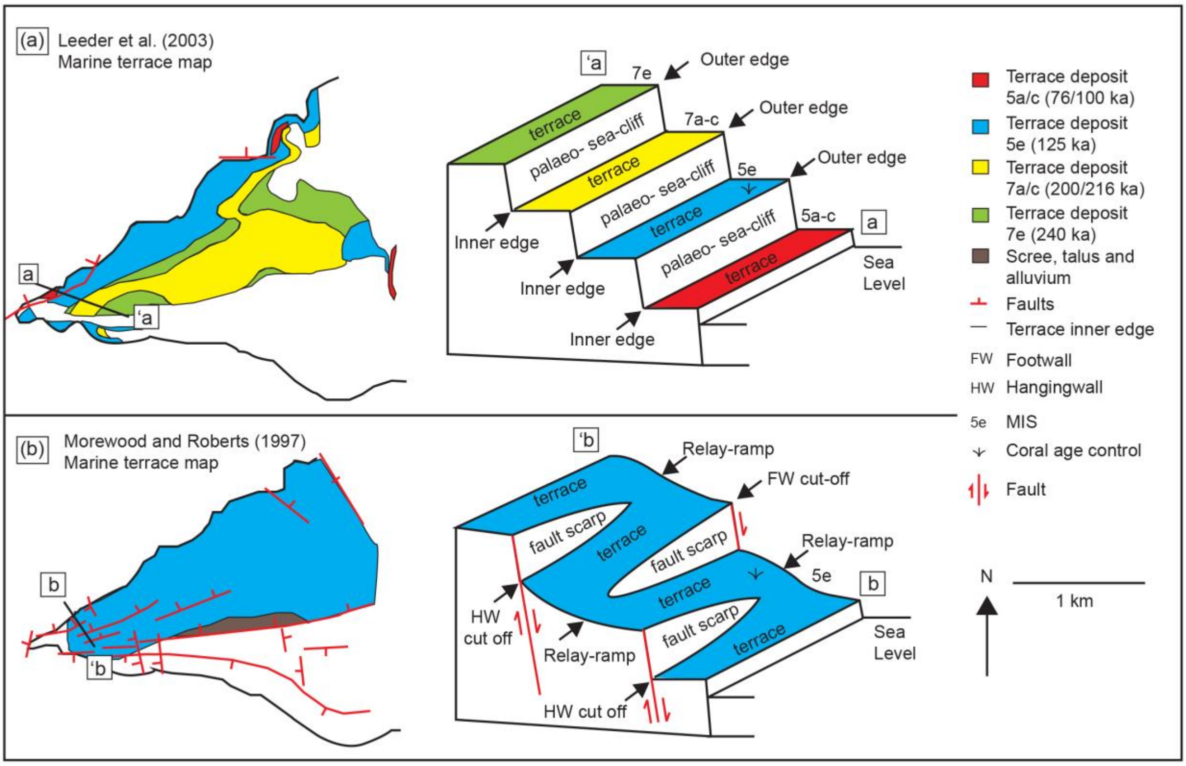

Figure 3: Comparison of two explanations for the observed geomorphology on Cape Heraion. (a) Geological map redrawn from Leeder et al. (2003) and interpreted schematic 3D diagram, Leeder et al. (2003) suggest a sequence of palaeoshorelines from MIS 5a/c (76.5 ka/100 ka) to 7e (240 ka). (b) Geological map redrawn from Morewood and Roberts (1997) and interpreted schematic 3D diagram, Morewood and Roberts (1997) suggest Cape Heraion is linked to the MIS 5e 125 ka highstand and has been latterly faulted.

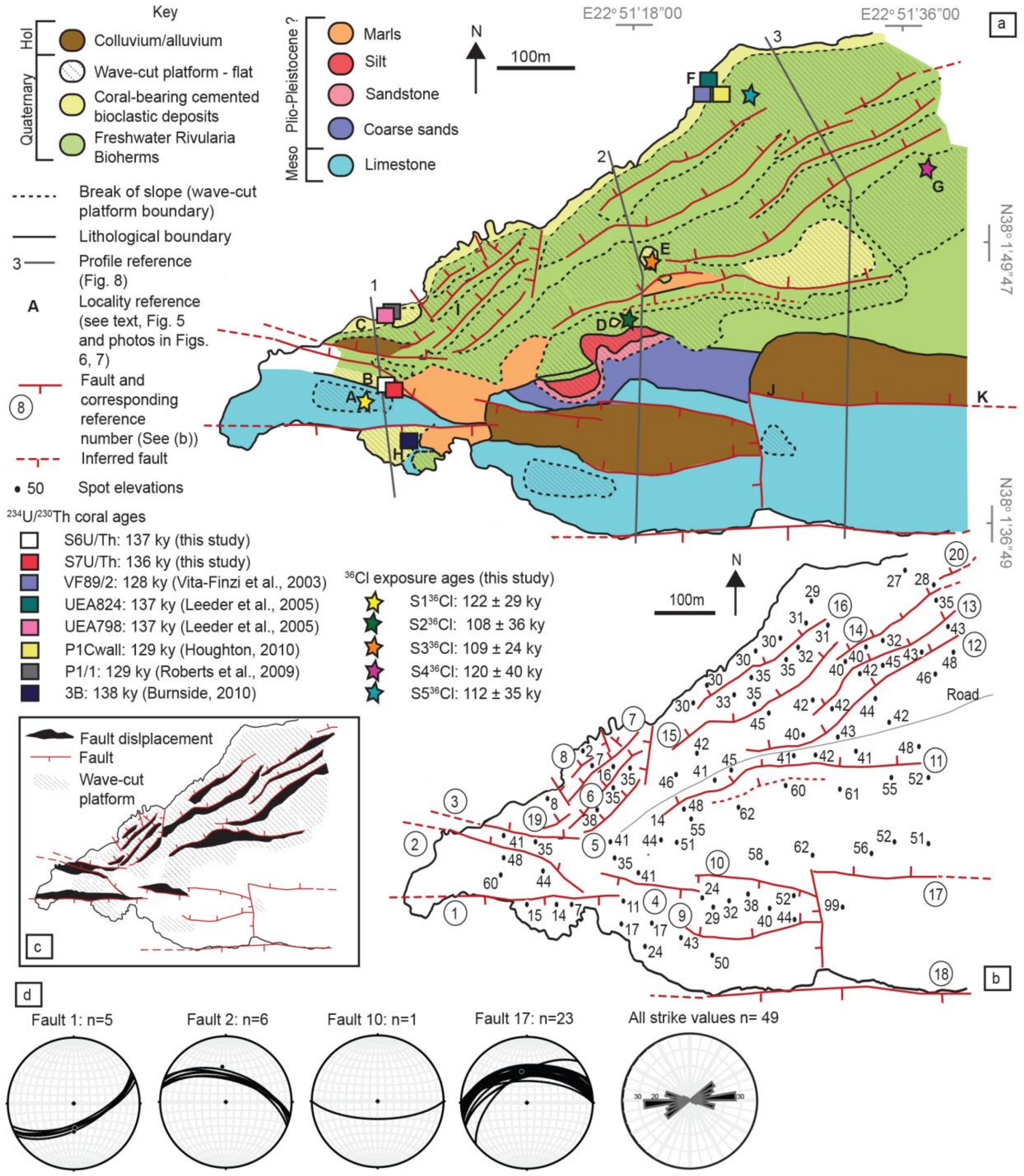

Figure 4: (a) Geological and geomorphological map of Cape Heraion, age controls from this study and other coral studies (Vita-Finzi et al., 2003; Leeder et al., 2005; Roberts et al., 2009; Burnside, 2010; Houghton, 2010). (b) Fault map of Cape Heraion and spot height elevations used to plot the fault displacement in (c). (d) Stereonet plots for faults 1, 2, 10 and 17, rose diagram representing all measured strike values.

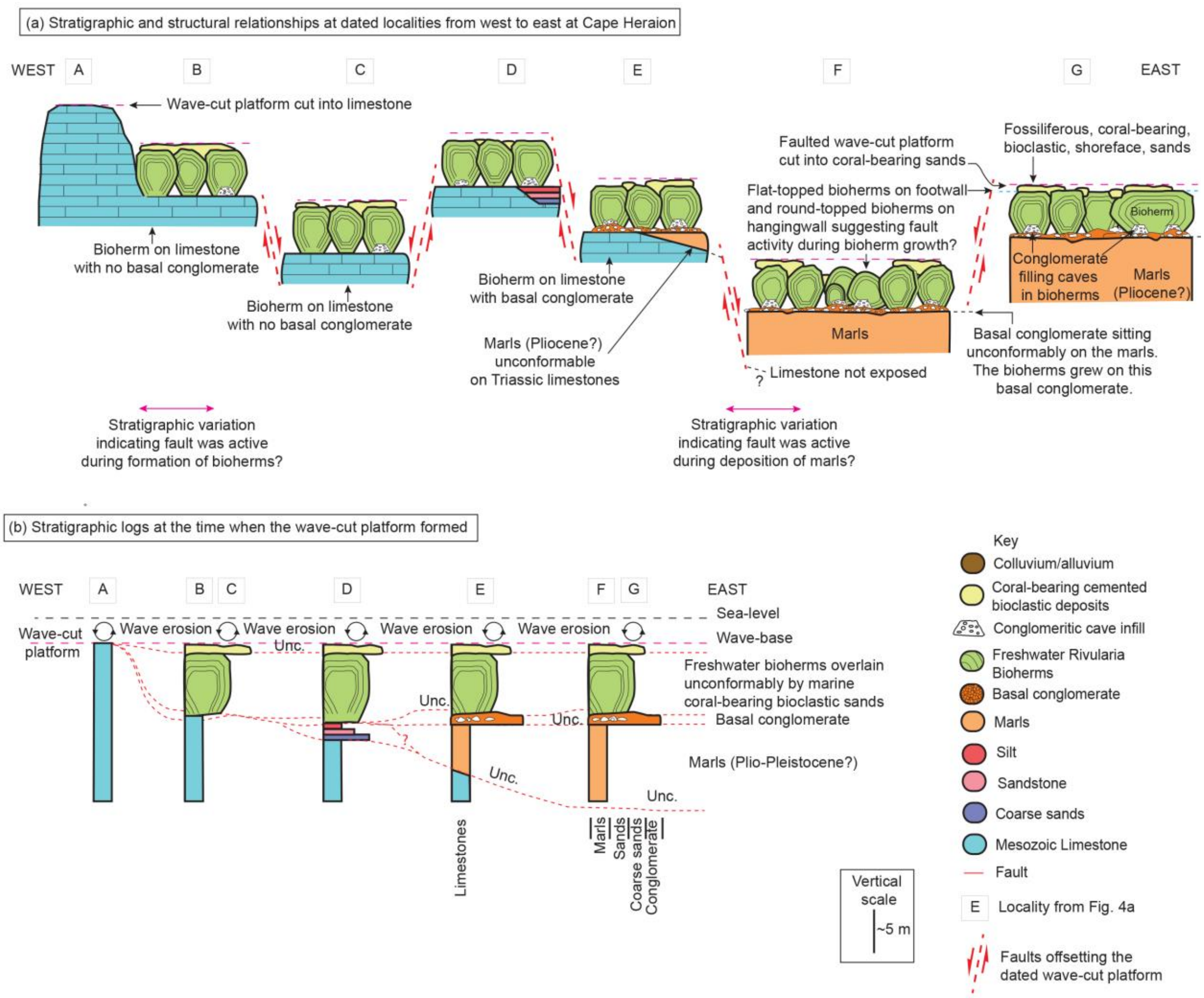

Figure 5: (a) Stratigraphic and structural relationships and (b) stratigraphic logs for dated localities from West to East, see Figure 4 for localities

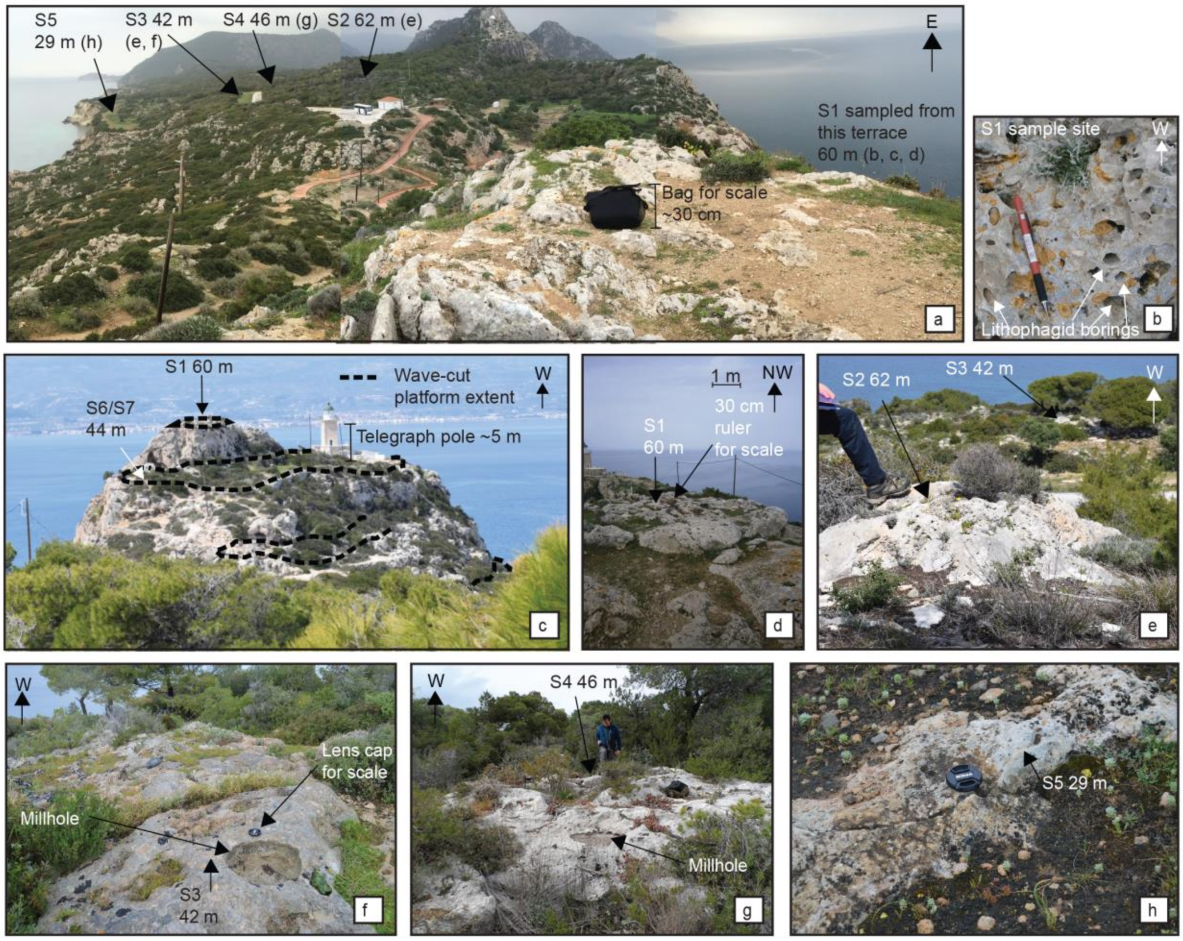

Figure 6: (a) overview of ^{36}Cl sample locations. (b-h) Photographs of ^{36}Cl and ^{234}U/^{230}Th sample locations. See Figure 4a for locations of samples.

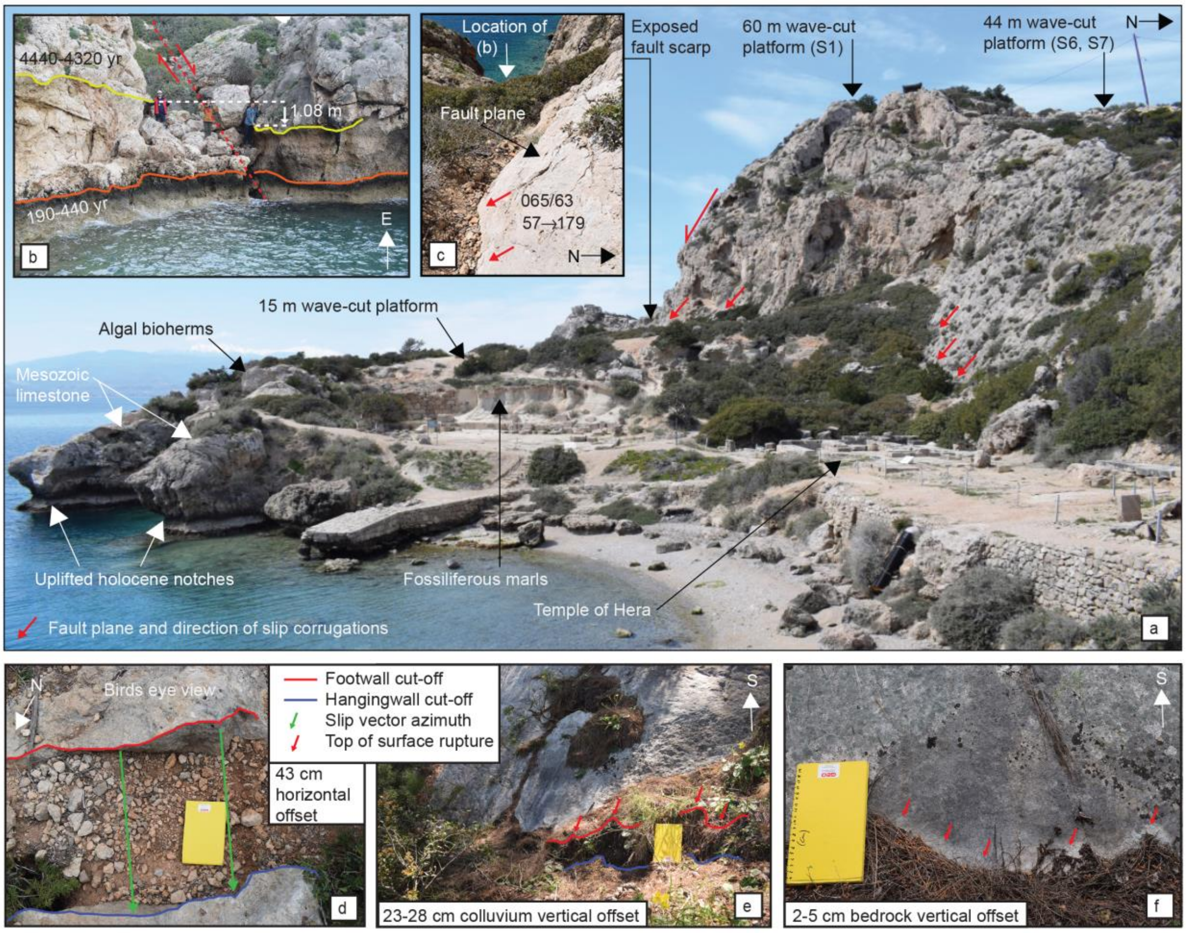

Figure 7: (a) View of Fault 1 offsetting a wave-cut platform at 60 m and 15 m. (b) Annotated photograph of offset wave-cut notches on Fault 1. (c) Fault plane and annotated direction of fault slip for Fault 1. (d) North-south horizontal offset of 43 cm on a bioherm on the north side of Cape Heraion at Locality I, Figure 4. Offset colluvium (e) and bedrock (f) along fault 17 between localities J and K, Figure 4, UTM location: 663350/4210630.

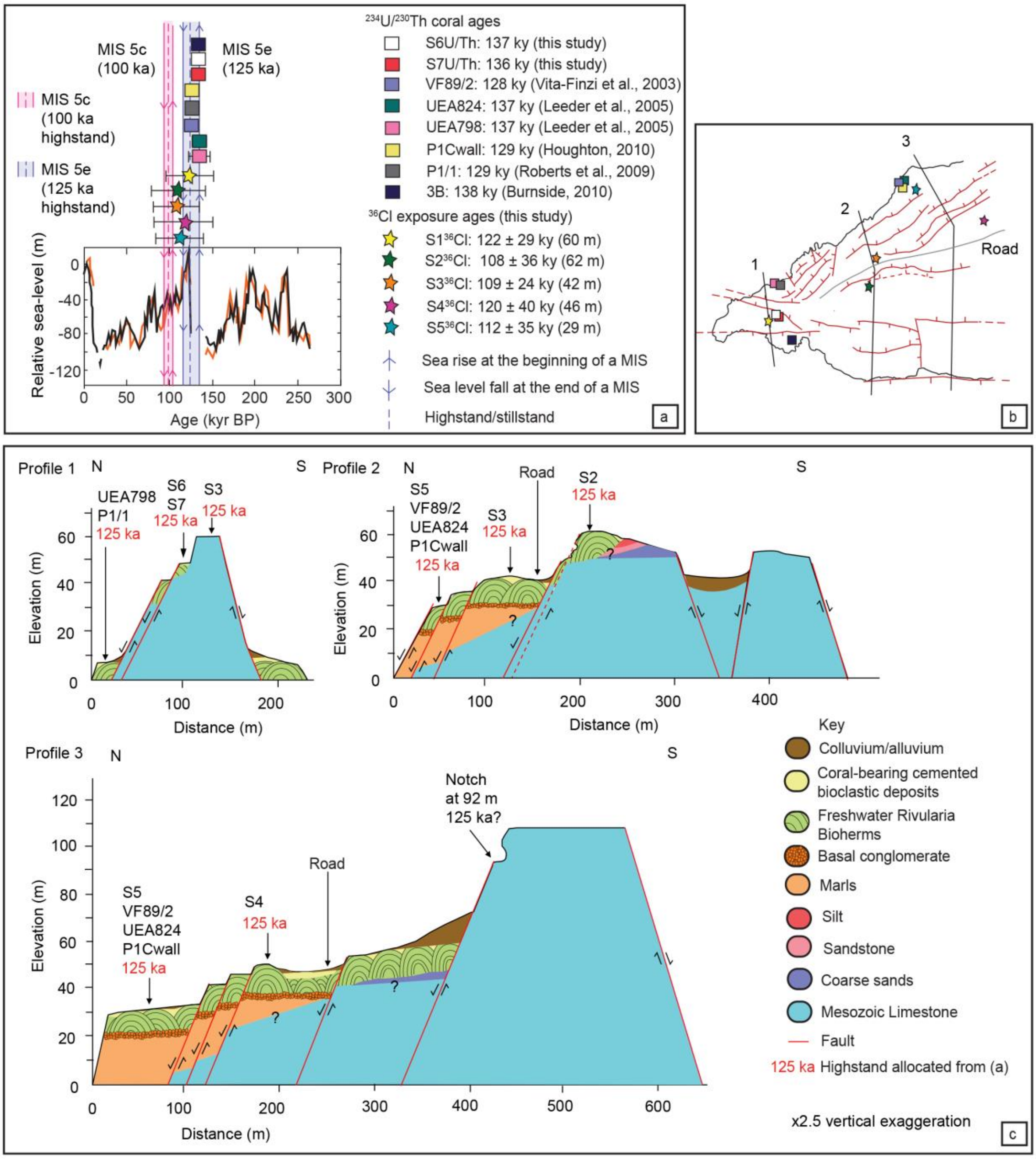

Figure 8: (a) ^{36}Cl exposure ages and ^{234}U/^{230}Th coral ages (where error bars are not visible, the value of error is smaller than the plot marker). Ages are plotted against the sea level curve from Siddall et al., 2003, orange and black lines represent different cores used to construct the sea-level curve. (b) Fault map and the location of profile lines from Figures 4a, b that are shown as schematic cross sections in (c).

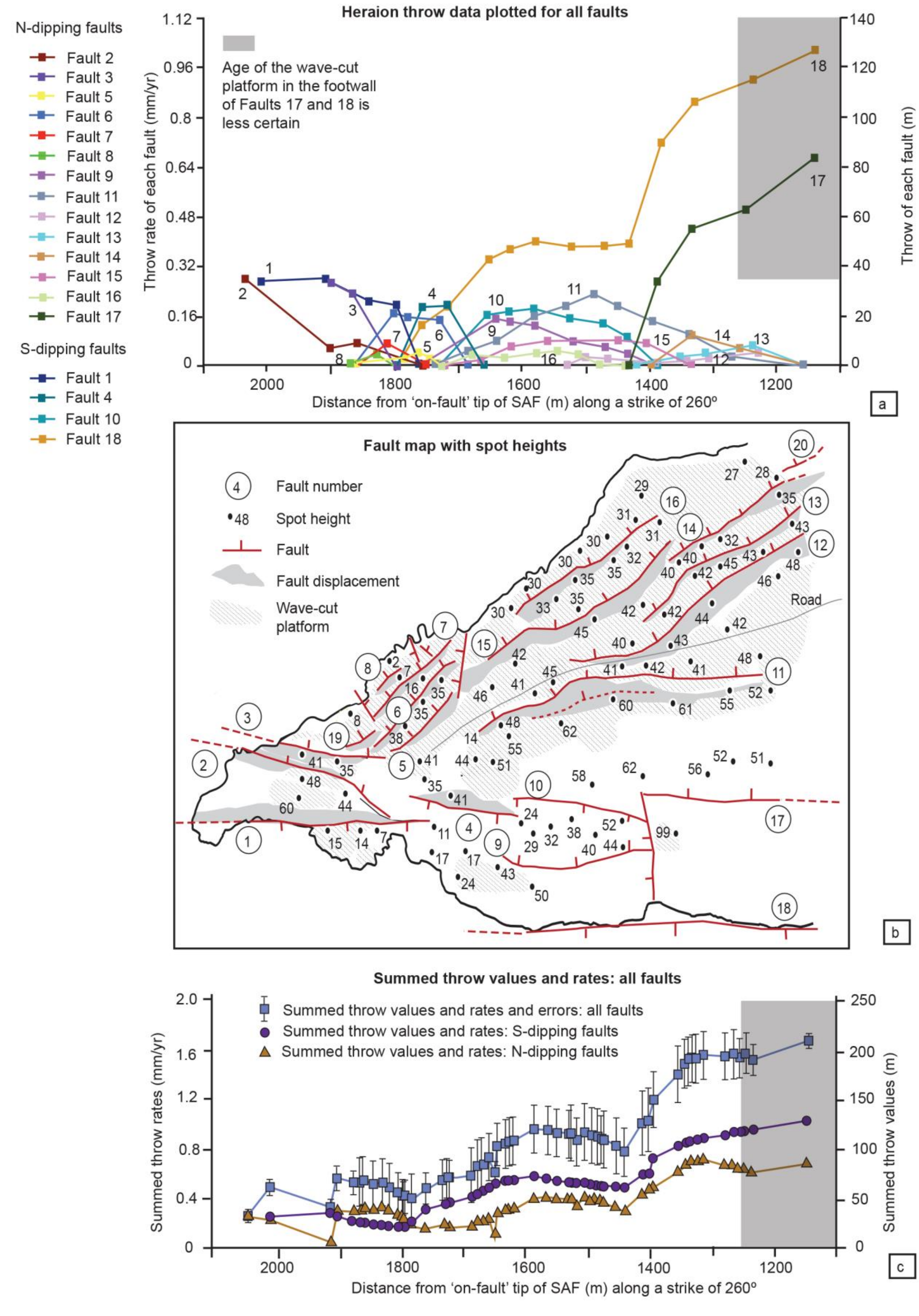

Figure 9: (a) Throw profiles for individual faults constructed using elevation data (shown in (b)). Throw values for Fault 19 is not plotted owing to a lack of elevation data. (c) Summed

throw values and rates for all faults with uncertainties, summed throw values for north- and south-dipping faults. For (a) and (c) throw for each fault is plotted against the distance from the 'on-fault' tip (A) shown in Figure 2c from Morewood and Roberts (1999).

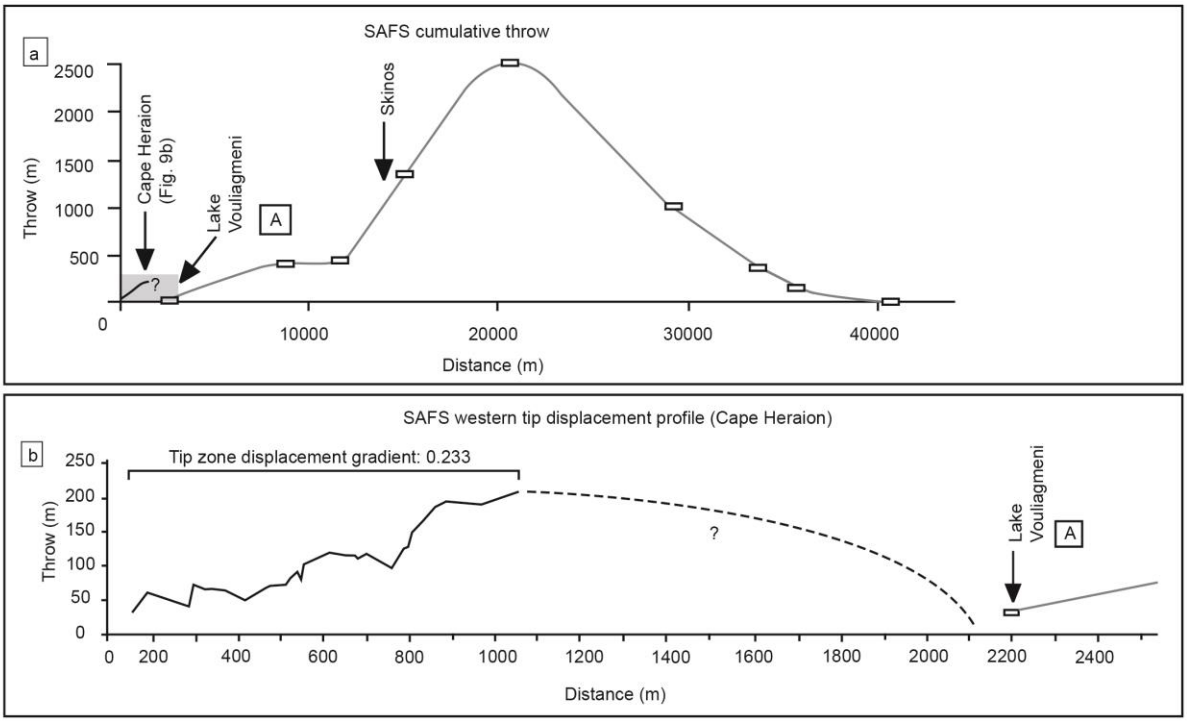

Figure 10: (a) Summed throw of Cape Heraion faults plotted alongside cumulative throw of the SAFS (modified from Morewood and Roberts (1999)). (b) Tip zone throw and displacement gradient from Cape Heraion. See Figure 2c for the location of A ('on-fault' tip of the SAFS).

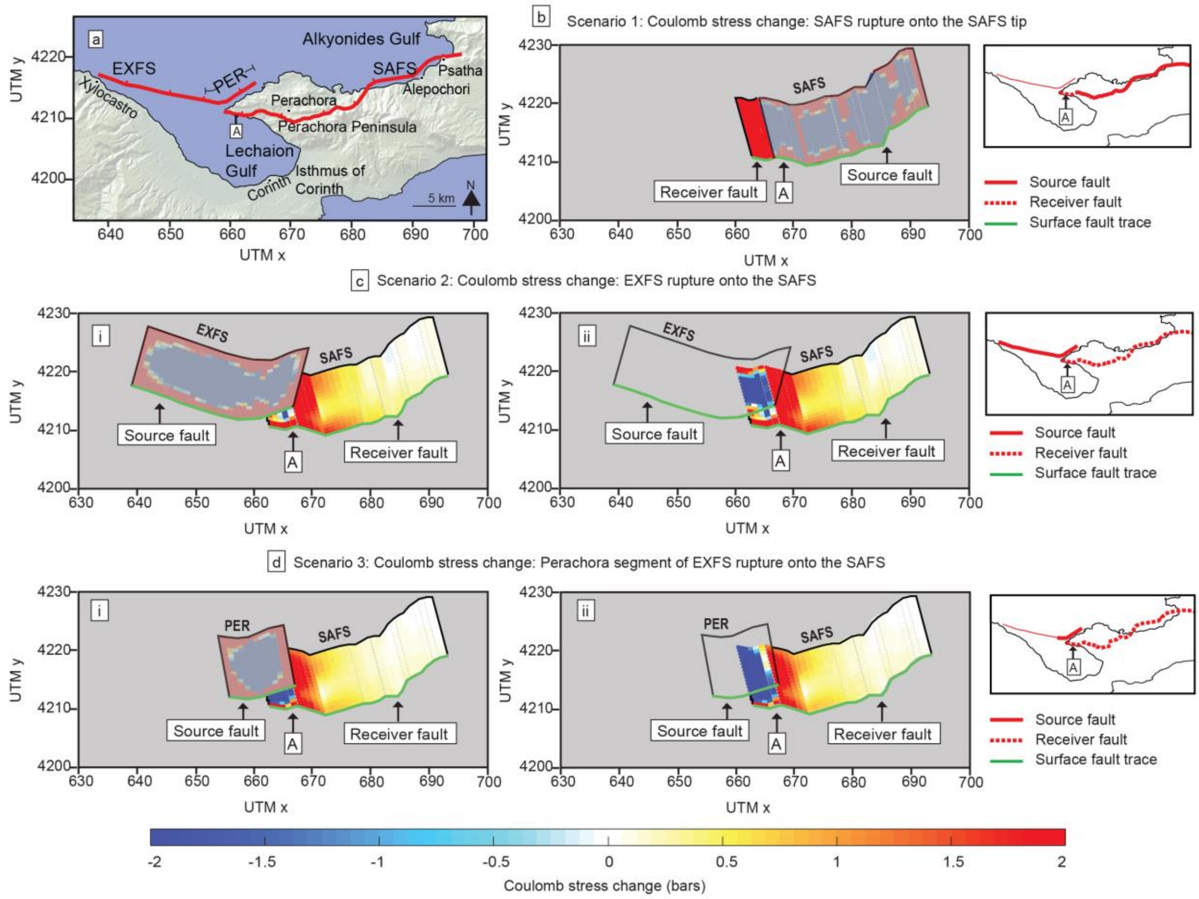

Figure 11: (a) Map of eastern Gulf of Corinth showing the fault traces modelled in Coulomb stress change (b-d) for the South Alkyonides Fault System (SAFS) and East Xylocastro Fault System (EXFS) (adapted from Figure 2a). See table 4 for inputs into Coulomb modelling. (b) Coulomb stress change from rupturing the source fault (entire SAFS with the exception of the western 5 km) onto the receiver fault (western 5 km section of the SAFS). (c) Coulomb stress change from rupturing the source fault (entire EXFS) onto the receiver fault (SAFS), (i) shows the source fault rupture, (ii) shows the source fault outline only. (d) Coulomb stress change from rupturing the source fault (Perachora segment of the EXFS) onto the receiver fault (SAFS), (i) shows the source fault rupture, (ii) shows the source fault outline only.

Fault number	d/L ratio
4	0.27
5	0.04
6	0.10
7	0.06
8	0.08
9	0.05
10	0.08
11	0.04
12	0.01
13	0.02
14	0.06
15	0.03
16	0.03

Table 1: displacement length (d/L) ratios for mapped faults on Cape Heraion, with the exception of Fault 19 due to a lack of elevation data and Faults 1, 2, 3, 17, 18, 20 as both tips could not be mapped.

Sample name	Lab ID	UTM		Sampling elevation (m)	Age (ky)	±2s (abs) (ky)	U (ppm)	^{232}Th (ppb)	(^{230}Th/ ^{232}Th)	(^{232}Th/ ^{238}U)	±2s (%)	(^{230}Th/ ^{238}U)	±2s (%)	(^{234}U/ ^{238}U)	±2s (%)	δ234U	±2s (%)
		Easting	Northing														
S6U/Th (1)	138-34	662540	4210594	44	133.5	0.7	2.42	0.005	1210.7	0.00068	0.04	0.81787	0.25	1.1354	0.14	197	±2
S6U/Th (2)	141-29	662540	4210594	44	135.4	1.2	2.44	0.006	1073.3	0.00076	0.12	0.82081	0.35	1.1315	0.28	193	±4
S6U/Th (3)	141-30	662540	4210594	44	142.7	1.3	2.57	0.006	1074.0	0.00079	0.10	0.85306	0.34	1.1429	0.25	214	±4
S6U/Th (4)	145-12	662540	4210594	44	173.7	2.0	2.13	0.009	674.9	0.00136	0.17	0.92101	0.34	1.1287	0.29	210	±5
S7U/Th (1)	138-35	662540	4210594	44	140.8	0.8	2.26	0.008	736.1	0.00114	0.04	0.83619	0.22	1.1298	0.13	193	±2
S7U/Th (2)	145-13	662540	4210594	44	139.1	0.9	2.28	0.012	467.2	0.00179	0.08	0.83630	0.25	1.1359	0.18	201	±3
S7U/Th (3)	145-14	662540	4210594	44	135.2	1.0	2.24	0.009	599.5	0.00137	0.10	0.81931	0.29	1.1301	0.21	191	±3
S7U/Th (4)	145-15	662540	4210594	44	134.5	1.0	2.34	0.014	426.6	0.00192	0.11	0.81943	0.29	1.1328	0.22	194	±3
S7U/Th (5)	145-16	662540	4210594	44	134.7	0.9	2.13	0.008	658.4	0.00125	0.09	0.82413	0.26	1.1380	0.19	202	±3
S7U/Th (6)	145-17	662540	4210594	44	132.3	0.9	2.39	0.016	364.2	0.00223	0.08	0.81141	0.29	1.1315	0.21	191	±3

Table 2: 234U/230Th coral age dating analytical results for samples S6U/Th and S7U/Th (see Figure 4a for sample location). Activity ratios calculated using the 234U and 230Th decay constants of Cheng et al. 2013. Activity ratios corrected for 230Th, 234U and 238U contribution from the synthetic 236U-229Th tracer, instrument baselines, mass bias, hydride formation and tailing. 230Th blanks amounting to 0.15 ± 0.03 fg were subtracted from each sample. 238U blanks were on the order of 10 pg, and were negligible relative to sample size. Age and δ234U data were corrected for the presence of initial 230Th assuming an initial isotope composition of (232Th/238U) = 1.2 ± 0.6, (230Th/238U) = 1 ± 0.5 and (234U/238U) = 1 ± 0.5 (all uncertainties quoted at the 2σ level).

Sample name	Lithology and geomorphology	Latitude	Longitude	Elevation	Lithology	Erosion rate (mm/ky)	Total erosion (cm)	Cl (ppm)	±	^{36}Cl (atoms/g)	±	CaO (wt%)	±	Age (kyr)	Internal uncertainty (kyr)	External uncertainty (kyr)
1	Limestone: flat WCP with lithophagid borings. Sample removed from the the area displaying lithophagid borings (Fig. 6b)	38.0288	22.85106	60	Limestone	0.1	1.2	17.0503	0.2856	2327699	63421	57.41	1.38	122	3.7	29
2	Bioherm top, bioclastic sands infill spaces between adjacent bioherms. Sample removed from the top iof the bioherm (Fig. 6e)	38.0292	22.85297	62	Bioherm	6	64.8	22.5328	0.4739	1195064	34923	43.85	1.53	108	8.4	36
3	Bioclastic packstone, excellent millholes preserved. Ssample removed from immediately adjacent to the millhole (Fig. 6f)	38.0304	22.85522	42	Packstone	0.1	1.1	38.7794	0.8003	1887336	54970	49.02	1.52	109	3.5	24
4	Bioherm top, millholes, abundant lithophagid borings preserved on the adjacent backwall (Fig. 6g)	38.032	22.8596	46	Bioherm	6	72.0	33.3263	0.6646	1616569	47009	53.80	1.47	120	8.8	40
5	Bioherm top, visible above surrounding alluvium (Fig. 6h)	38.0305	22.85516	29	Bioherm	6	67.2	60.5561	1.6227	1684932	46140	54.01	1.44	112	9.3	35

Table 3: ^{36}Cl exposure dating analytical results and sample descriptions (see Figure 4a for the sample location). ^{36}Cl concentrations are based on 1.2x10^{-12} ^{36}Cl/Cl ratio for Z93-0005 (PRIME Lab, Purdue). This standard agrees with standards prepared by K. Nishiizumi, which were used as secondary standards. Cl concentrations were determined by AMS isotope dilution (Stuart and Dunai, 2009). ^{36}Cl/Cl processed blank ratios ranged between 2.4 and 6.03% of the samples ^{36}Cl/Cl ratios.

Fault name	Fault information (fault trace, kinematics)	Length (km)	Depth of seismogenic zone (km)	Dip º	Facing direction º	Rake º	Sub-surface maximum slip value (m)	Max. Mw	Figure
East Xylocastro Faut System (EAFS)	Whole fault length is used combining fault traces of the East Xylocastro Fault, North Kiato Fault and Perachora Fault as per Nixon et al., 2016.	29	15	55	010	-90	1.6	6.53	11b
Perachora Fault (EXFS)	Fault trace from Nixon et al., 2016	11	15	55	350	-90	1.4	6.21	11c
South Alkyonnides Fault System (SAFS)	Whole fault length is used as per Roberts et al., 2009 (rupturing the Pisia, East Alkyonides and Psatha faults), with the exception of western 5 km tip zone. Dip data averaged from Jackson et al., 1982 (45˚) and Mechernich et al., 2016 (60˚)	38.7	15	55	345	-90	2.4	6.74	11a

Table 4: Inputs for Coulomb stress change modelling. Slip at the surface is set at 0.1 (10%) of the slip value at depth. This value is based upon the relationship between surface slip (Vittori et al., 2011) and maximum slip values at depth (Wilkinson et al., 2015) for the Mw 6.3 2009 L'Aquila Earthquake, Italy

Supplementary 1:

Description of the observed stratigraphy on Cape Heraion to accompany Figures 4a and 5)

At the base of the stratigraphic column is Mesozoic limestone (Figures 4a, 5, Locality A). Unconformably above the limestone is a sedimentary succession, only observed in the centre of the cape, that fines up from coarse sands to silts (Locality D, Figure 4a and Figure 5). Plio-Pleistocene marls are inferred to occur stratigraphically above the sands and silts although the contact between them has not been observed, and they may be lateral equivalents. The marls form large cliff outcrops along the north of the cape (e.g. Locality F in Figures 4 and 5) and are overlain by a coarse boulder conglomerate that displays an erosive base cut into the underlying marls (Locality F). Algal carbonate bioherms formed of *Rivularia haematities* have grown on the basal conglomerate (Localities E, F and G, Figure 5) and directly on the basement limestone (Localities B, C and D, Figure 5). In turn, the bioherms are overlain by fossiliferous, coral-bearing, marine bioclastic sands preserved as a continuous 0.6-1.0 m thick layer (Localities B, C, E, F and H, Figures 4a, 5) or as patches infilling cavities between or within the bioherms (Locality C and D Figure 4a, 5). These bioclastic deposits have rich fossil assemblages with colonies of the branching coral *Cladocora caespitosa* in life position, frameworks of serpulid worm tubes, and bivalves, pecten, turritella, bryozoa, and elsewhere broken fragments of *Cladocora caespitosa* within the sediment that form death assemblages. In places, the inside of the bioherms has been eroded and small caves have formed, which have been bored by lithophagids (Figure 5). The caves contain marine deposits such as *Cladocora caespitosa* (e.g. Locality C), suggesting the cave-filling deposits are the age-equivalents of the coral-bearing bioclastic sands that lie on top of the bioherms.

Supplementary 2

1: Sample Name	2: Scaling (Select One)	3: Latitude decimal degrees	4: Longitude decimal degrees	5: Elevation meters	6: Pressure hPa	7: Atmospheric Pressure or Elevation	8: Sample Thickness cm	9: Bulk Density g/cm 3	10: Shielding Factor unitless	11: Erosion Rate mm/kyr	12: Conc. 36Cl Atoms of 36 Cl/g of sample	13: Attenuation length g/cm 2	14: Depth to Top of Sample g/cm 2	15: Year Collected Year A.D.	16: Water Content in Pores volume fraction	17: Mineral Separation (Select One)	18: Bulk Rock SiO2 oxide weight %	19: Bulk Rock TiO2 oxide weight %	20: Bulk Rock Al2O3 oxide weight %
1	DE	38.02877	22.851055	60		Elevation	3.7	2.649	0.9999	0.1	2327699	160	0	2000	0.01	No	0	0	0
2	DE	38.02919	22.852974	62		Elevation	4	2.565	0.9999	6	1195064	160	0	2000	0.01	No	0	0	0
3	DE	38.03036	22.855224	42		Elevation	3.4	2.565	0.9981	0.1	1887336	160	0	2000	0.01	No	0	0	0
4	DE	38.03203	22.859599	46		Elevation	4.5	2.233	0.9999	6	1616569	160	0	2000	0.01	No	0	0	0
5	DE	38.03046	22.855155	29		Elevation	4.1	2.565	0.9995	6	1684932	160	0	2000	0.01	No	0	0	0

21: Bulk Rock Fe2O3 oxide weight %	22: Bulk Rock MnO oxide weight %	23: Bulk Rock MgO oxide weight %	24: Bulk Rock CaO oxide weight %	25: Bulk Rock Na2O oxide weight %	26: Bulk Rock K2O oxide weight %	27: Bulk Rock P2O5 oxide weight %	28: Analytical Water weight %	29: Bulk Rock CO2 oxide weight %	30: Bulk Rock Cl ppm	31: Bulk Rock B ppm	32: Bulk Rock Sm ppm	33: Bulk Rock Gd ppm	34: Bulk Rock U ppm	35: Bulk Rock Th ppm	36: Bulk Rock Cr ppm	37: Bulk Rock Li ppm	38: Target K2O weight %	39: Target CaO weight %	40: Target TiO2 weight %
0.05148	0	0.00	57.38099	0	0.00000	0	1.00000	42.56753	17.05027	0	0	0	0	0	0	0	0.00000	57.41238	0.00000
0.02843	0	0.00	43.82164	0	0.00000	0	1.00000	56.14993	22.5328	0	0	0	0	0	0	0	0.00000	43.84561	0.00000
0.061312	0	0.00	48.98905	0	0.00000	0	1.00000	50.94964	38.77938	0	0	0	0	0	0	0	0.00000	49.01585	0.00000
0.02793	0	0.00	53.77027	0	0.00000	0	1.00000	46.20180	33.32635	0	0	0	0	0	0	0	0.00000	53.79968	0.00000
0.120106	0	0.00	53.98398	0	0.00000	0	1.00000	45.89592	60.55609	0	0	0	0	0	0	0	0.00000	54.01351	0.00000

41: Target Fe2O3 weight %	42: Target Cl ppm	43: Latitude Uncertainty decimal degrees	44: Longitude Uncertainty decimal degrees	45: Elevation Uncertainty meters	46: Pressure Uncertainty hPa	47: Sample Thickness Uncertainty cm	48: Bulk Density Uncertainty g/cm 3	49: Shielding Factor Uncertainty unitless	50: Erosion-Rate Uncertainty mm/kyr	51: Conc. 36 Cl Uncertainty Atoms of 36 Cl/g of sample	52: Attenuation Length Uncertainty g/cm 2	53: Depth to Top of Sample Uncertainty g/cm 2	54: Year Collected Uncertainty Year A.D.	55: Water Content in Pores Uncertainty Volume %	56: Bulk Rock SiO 2 Uncertainty oxide weight %	57: Bulk Rock TiO 2 Uncertainty oxide weight %	58: Bulk Rock Al 2 O 3 Uncertainty oxide weight %	59: Bulk Rock Fe 2 O 3 Uncertainty oxide weight %	60: Bulk Rock MnO Uncertainty oxide weight %
0.05148	17.05	0	0	10		0.5	0.2	0	0	63421	10	0	10	0.01	0	0.0000	0	0.46670195	0
0.02843	22.53	0	0	10		0.5	0.2	0	0	34923	10	0	10	0.01	0	0.0000	0	0.51572725	0
0.061312	38.78	0	0	10		0.5	0.2	0	0	54970	10	0	10	0.01	0	0.0000	0	0.51356044	0
0.02793	33.33	0	0	10		0.5	0.2	0	0	47009	10	0	10	0.01	0	0.0000	0	0.49714071	0
0.120106	60.56	0	0	10		0.5	0.2	0	0	46140	10	0	10	0.01	0	0.0000	0	0.48551267	0

61: Bulk Rock MgO Uncertainty oxide weight %	62: Bulk Rock CaO Uncertainty oxide weight %	63: Bulk Rock Na 2 O Uncertainty oxide weight %	64: Bulk Rock K 2 O Uncertainty oxide weight %	65: Bulk Rock P 2 O 5 Uncertainty oxide weight %	66: Analytical Water Uncertainty weight %	67: Bulk Rock CO 2 Uncertainty oxide weight %	68: Bulk Rock Cl Uncertainty ppm	69: Bulk Rock B Uncertainty ppm	70: Bulk Rock Sm Uncertainty ppm	71: Bulk Rock Gd Uncertainty ppm	72: Bulk Rock U Uncertainty ppm	73: Bulk Rock Th Uncertainty ppm	74: Bulk Rock Cr Uncertainty ppm	75: Bulk Rock Li Uncertainty ppm	76: Target K2O Uncertainty weight %	77: Target CaO Uncertainty weight %	78: Target TiO2 Uncertainty weight %	79: Target Fe2O3 Uncertainty weight %	80: Target Cl Uncertainty ppm	81: Covariance unitless
0	1.3804232	0	0.0000	0	1.00000	1.3804232	0.28561763	0	0	0	0	0	0	0	0.00000	1.3804232	0.00000	0.46670195	0.28561763	0
0	1.5254315	0	0.0000	0	1.00000	1.5254315	0.47391526	0	0	0	0	0	0	0	0.00000	1.5254315	0.00000	0.51572725	0.47391526	0
0	1.51902247	0	0.0000	0	1.00000	1.51902247	0.80026479	0	0	0	0	0	0	0	0.00000	1.51902247	0.00000	0.51356044	0.80026479	0
0	1.47045576	0	0.0000	0	1.00000	1.47045576	0.66456149	0	0	0	0	0	0	0	0.00000	1.47045576	0.00000	0.49714071	0.66456149	0
0	1.43606203	0	0.0000	0	1.00000	1.43606203	1.62273089	0	0	0	0	0	0	0	0.00000	1.43606203	0.00000	0.48551267	1.62273089	0

Supplement 2: Input data for CRONUScalc to determine ages of ^{36}Cl exposure samples

Supplementary 3

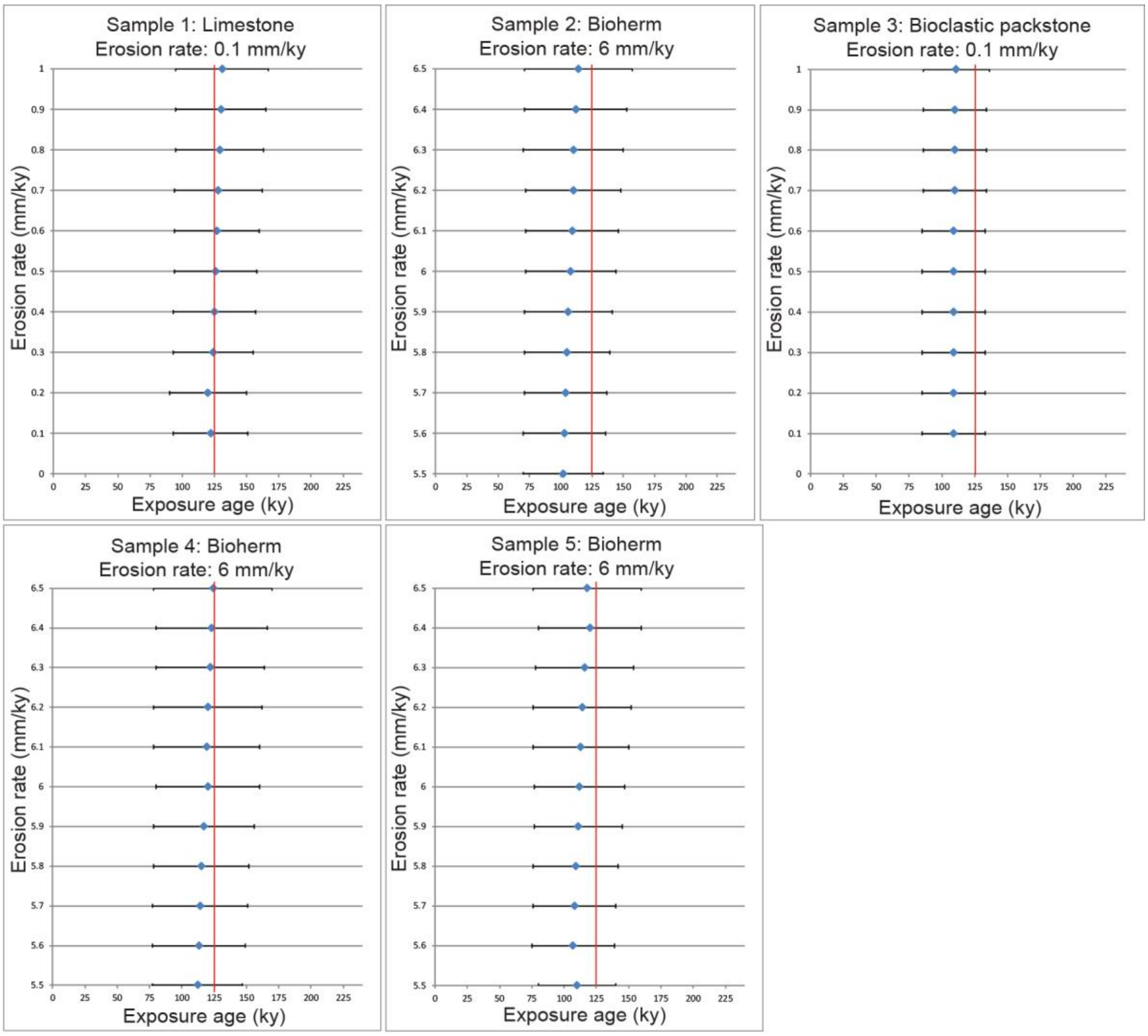

Supplement 3: Sensitivity tests for the erosion rates of 0.1-1.0 mm/ky for samples 1 and 3, and of 5.5-6.5 mm/yr for samples 2, 4 and 5.